Deep Slab Seismicity Limited by Rate of Deformation in the Transition Zone

Magali I. Billen

Department of Earth and Planetary Sciences

University of California, Davis

Short title: Strain-rate Limited Deep Slab Seismicity

Abstract: Deep earthquakes within subducting lithosphere (slabs) have remained enigmatic because of their similarities with shallow earthquakes and the high pressures at which they occur. Previous attempts to explain the global depth distribution of deep earthquakes, in terms of the thermal conditions at which possible triggering mechanisms are viable, fail to explain the variability in seismicity within and between slabs. In addition to thermal constraints, the proposed failure mechanisms for deep earthquakes all require that sufficient strain accumulates in the slab at a high enough level of stress. Here I show that simulations of subduction with non-linear rheology and compositionally-dependent phase transitions, exhibit strongly variable strain-rate magnitude in space and time, which is similar to observed seismicity strain-rate depth profiles. I argue that, in addition to one of the possible deep earthquake triggering mechanisms, variations in strain-rate determine the spatially-variable distribution of deep earthquakes and explains why there are large gaps in seismicity (low strain-rate), variable peaks in seismicity (high strain-rate bending regions)

and, possibly, an abrupt cessation of seismicity below 660 km.

Introduction

Deep earthquakes occur within cold (< 900–1000°C) slabs at pressures of 10–25 GPa (350–680 km). At these high pressures brittle failure by frictional sliding or fracture, as occurs near the surface of the Earth, is inhibited. Therefore, brittle failure at these high pressures requires a different mechanism to either overcome the large normal stresses (e.g., embrittlement through high pore fluid pressure) or a weakening mechanism. Therefore, much of the research on deep earthquakes has focused on the conditions at which sufficient fluids are present for embrittlement to occur (*1, 2*) or on the conditions at which weakening mechanisms can trigger failure. Other proposed failure mechanisms include thermal shear instability (*3–5*) and transformational faulting of metastable olivine (MO) (*6, 7*) or pyroxene (*8*), both of which trigger faulting through localized weakening. However, at both low and high pressure, the rock must be at conditions where strain energy accumulates and can be released through the failure processes. This study is focused on better understanding the physical conditions that determine where sufficient strain energy accumulates and how those conditions are related to the observed spatial distribution of seismicity.

Despite the differences in pressure-temperature conditions and triggering mechanisms, seismological observations of deep earthquakes suggests that these events are similar to shallow events in several ways. Deep earthquakes have (mostly) double-couple mechanisms indicating that they occur as a shear failure, aftershock sequences follow a standard Omori Law for aftershock decay, energy/moment ratios are similar to shallow events, and long-range triggering of deep earthquakes has been observed (for comprehensive reviews see (*9–11*)). Analysis of source-time functions also

show remarkable similarity between shallow and deep earthquakes when depth-dependent differences in rigidity are taken into account (*12*).

However, compared to shallow events, deep earthquakes tend to have shorter rupture duration for a given earthquake size, exhibit more rupture complexity (i.e., multiple subevents), have a larger range in stress drop (1–100s MPa) and rupture velocities (0.2–0.9 times shear velocity; with some earthquakes exhibiting supershear rupture velocity: see references in (*11*)), and exhibit depth dependent aftershock productivity (e.g., almost absent at intermediate depths, but higher deeper than 550 km). In addition, some very deep events have very low radiation efficiency (< 0.1), which has been interpreted to indicate melting during the rupture process (*13*). These seismic observations indicate that the rupture process for shallow and deep earthquakes is similar (i.e., a shear failure), despite different failure mechanisms and physical conditions (P-T, deviatoric stress) which affect the details of the rupture process and strain energy release.

Seismicity in the subducting lithosphere is often presented as the number of earthquakes per year versus depth for the world's subduction zones (i.e., the global slab seismicity-depth profile; Figure 1A). This profile has been interpreted as indicating that there are likely two mechanisms for slab earthquakes, with dehydration embrittlement occurring at intermediate depths (50–300 km) where fluids are being released from the slab, and transformational faulting occurring deeper, where the slab is likely drier and metastable olivine or pyroxene may be present. There is growing seismological evidence for a metastable olivine wedge in the Japan slab, although it has not been definitively detected elsewhere due to a lack of dense seismic networks above other slabs (*11*). In addition, Gutenberg-Richter statistics (i.e., b-values) also differ for seismicity above and below 350 km supporting the hypothesis that there are two different mechanisms (*9*).

This explanation for the depth-distribution of seismicity, based on a depth controlled failure

mechanism, needs to be re-evaluated in light of new observations. First, there is growing evidence that the deep slab may not be dry and fluids can be transported and released from the slab in the deep transition zone (*14*). Second, regional differences in b-values suggest that rupture may occur by a combination of mechanisms including transformational faulting and thermal shear instability for deep earthquakes (*15*). Third, recent studies suggest that shear instability is also a viable mechanism for intermediate depth earthquakes (*4, 5, 16*).

All three proposed mechanisms for triggering deep earthquakes are to first-order controlled by the requirement that the slab remains sufficiently cold to the base of the transition zone. The thermal structure of slabs is primarily controlled by the age of the slab at the time of subduction (t_{sub}; older slabs are colder and thicker) and the rate at which slabs sink into the mantle (V_s; slower subduction allows more time for the slab to heat up). These two variables have been combined to define the thermal parameter, $\phi = V_s t_{sub}$, and compared to the maximum depth of seismicity in the slabs, z_{max}. This comparison has been shown to be consistent with the predicted depth extent of a MO wedge in kinematic thermal models (*17*) and in dynamic models (*18*), although thermal models accounting for the variability of thermal conductivity in the slab (*19*) or water effects on reaction kinetics (*20*) suggest the the MO wedge could be substantially shorter.

However, perhaps more problematic for any possible failure mechanism that is thermally limited is the observation that many slabs exhibit large gaps in seismicity below 410 km (see Figures S2–S9). Most notably, the Peru and Chile slabs, have earthquakes at 550–650 km, but no deep earthquakes from 410–550 km, and the same is true for sections of the Java-Sumatra slab. Similarly, the shallow-dipping section of the Japan slab (between profiles 3 and 4 in Figure S2Da) has a large aseismic region (~ 150 km across from 200 to 660 km depth).

These observations appear to be inconsistent with any mechanism for deep earthquakes that is

primarily controlled by temperature. This is because, temperature contours in the slab are elongate concentric surfaces, and therefore the critical temperature for the failure mechanism will be present at all depths up to the maximum depth. If earthquakes are occurring at 660 km because the slab is cold enough for the failure mechanism to operate at that depth, then there is a portion of the slab at all depths above 660 km that is also cold enough for earthquakes to occur. Large gaps in deep earthquake seismicity indicate that being cold enough for the deep earthquake failure mechanisms to be viable, while necessary is not a sufficient condition to explain the distribution of deep earthquakes. Therefore, some other physical factor, in addition to temperature, must control the depth distribution of deep earthquakes.

An alternative explanation for the peak in seismicity in the transition zone is that it is due to higher stresses in the slab at this depth caused by the viscous resistance in the lower mantle (*21*), buoyancy forces or stresses related to volume contraction associated with both equilibrium or metastable phase transitions (see (*22*) and references therein). These models demonstrate that the combination of available forces and slab rheology predicts high stress magnitudes (> 500 MPa). However, they are instantaneous calculations, which can not show if the resulting deformation of the slab is consistent with observations or occurs at high enough strain-rates. They also do not address the spatial variability in seismic strain-rate.

At shallow depths (< 100 km) in the crust and lithosphere, the interior of plates are aseismic, while seismicity occurs at plate boundaries where deformation is localized and strain-rates are high. Localized deformation at plate boundaries occurs through a feedback between tectonic forces and the rock rheology (e.g., (*23*)). High strain-rates are also known to be a factor affecting failure by thermal shear instability (*4*) and transformational faulting (*6*).This suggest that the discontinuous distribution of seismicity in slabs may also be determined by feedbacks between

the rheology and forces acting on the slab, which leads to a discontinuous distribution of high strain-rate regions in the cold slab.

Early consideration of the causes of deep earthquakes recognized that slab rheology is also an important factor in determining where deep earthquakes occur. Wortel (*24*) considered the requirement that the rheology of slabs must allow for the accumulation of stresses that are released in the process of an earthquake and used this to determine a critical temperature for deep seismicity of < 900–1000° C. Above this temperature the slab strength (viscosity) is too low and the stresses will be accommodated by viscous flow. This temperature is consistent with more recent estimates for the maximum temperature at which slabs deform through low temperature plasticity or yielding (*25*). Brodholt and Stein (*26*) later argued that slabs are rheologically strong enough to support deep earthquakes beyond 660 km, but assumed uniformly low strain-rate of 10^{-18} s^{-1} in the slab. At this low strain-rate, the slab would be essentially rigid and would sink through the mantle without deforming internally, which is inconsistent with the occurrence of earthquakes, and the deformed shapes of slabs inferred from seismicity (*27, 28*). Therefore, both the occurrence of earthquakes in slabs and the geometry of slabs require that slabs support relatively high stresses, but are able to deform internally. This is an important constraint, not just for the generation of deep earthquakes, but also for the rheology used in long-term subduction models.

The requirement that slabs support high stress and deform internally is met by dynamic models of subduction that employ a rheology with a strong temperature-dependence from a composite diffusion-dislocation creep viscosity for olivine and either yielding (e.g., (*29, 30*)) or some other approximation (*31*) of low temperature plasticity (*25*). Here I show that the strain-rate pattern within deforming slabs in such models varies spatially and temporally, and mimics the strong variability in seismicity within the world's subduction zones. I use this correspondence to argue

that observed seismic strain-rate, while only a fraction of the total strain-rate, reflects the actual variations in strain-rate in slabs. That is, in addition to the thermal constraints on the possible failure mechanisms, earthquakes occur where the strain-rate is high and the gaps in seismicity within cold slabs reflect regions of the slab that are deforming more slowly.

This is not an entirely new concept; Tao and O'Connell (*32*) showed that the peak in seismicity in the transition zone could be explained by the high strain-rate in a weak slab (same viscosity as the mantle) due to a jump in viscosity into the lower mantle. However, such a weak slab could not support the stresses required for earthquake generation, nor explain the magnitude or orientation of stress in the slab (*21*). More recently, others have shown that earthquakes preferentially align in regions of high curvature (e.g., (*27*)) and that weakening the slab leads to strain-rates in the deep slab that are sufficiently high to drive thermal shear instability (*33*). Here, I revisit this largely overlooked factor in the process of deep earthquake generation to explicitly argue that the seismicity distribution directly reflects the spatial variation in strain-rate within strong, but deforming slabs. Note, that this is different than arguing that seismicity occurs where the stresses are higher (e.g., (*21, 22*)): in fact, in the models presented, the stress within the cold slab is high everywhere because it is deforming at the yield stress (1 GPa), but a reduction in viscosity through plastic yielding allows the slab to deform at a higher strain-rate locally.

Results

The hypothesis presented here was first motivated by examining the strain-rate evolution in 2-D dynamic models of subduction, and noting the similarity to the seismicity pattern for intermediate to deep earthquakes. Therefore, I first present observed seismic strain-rate estimated from the

moment release rate in the slab (see Methods) and then compare this to the strain-rate distribution in slabs from simulations (see Methods and Supplementary Materials).

Seismic Strain-rate Depth Profiles

Although much consideration of the mechanisms for deep earthquakes have been motivated by the distinctive global seismicity depth profile (Figure 1A), there is considerable variability both between and within individual subduction zones. Figure 1B–I shows the regional seismicity and strain-rate profiles for 8 subduction zones. The strain-rate curves largely follow the seismicity pattern, except in regions with large events relative to the regional average, which exhibit strain-rate peaks (e.g., Kuriles at 600 km). There are three types of regional depth profiles. First, Tonga, Kermadec and Java-Sumatra are all similar to the global profiles with seismicity present at all depths, and a seismicity/strain-rate peak in the transition zone. Second, both Chile and Peru are distinctive due to the large gap in seismicity from 300 to 500 km (except for a few events in Chile). Finally, the Kuriles, Japan and Marianas lack the peak in the transition zone. In Japan there are only a few earthquakes deeper than 600 km, and the Marianas appears to have two peaks centered at 450 and 600 km.

The variability in seismicity and strain-rate observed between subduction zones is also present within individual subduction zones. Figures S2A–H show profiles spaced 100 or 200 km apart for all 8 subduction zones. Figure 2 shows the seismicity and strain-rate profiles for the central section of the Tonga-Kermadec slab from 32°S to 21°S. Even in this central region of an old (85–100 my) and cold slab, far from the effects of slab edges, the seismicity pattern and strain-rate vary significantly from one profile to the next. Some of the profiles have the characteristic peak

in seismicity within the transition zone, but the depth and width of the peak varies; still other profiles do not have this peak at all. In adjacent profiles the depth and width of the peak changes continuously, suggesting that the processes or conditions that determine the location of seismicity are also changing over length scales of less than 100 km along-strike.

The global average, while illustrative, does not capture the observed variability in seismicity and strain-rate. More importantly, ignoring this variability is ignoring important information about the conditions at which deep earthquakes occur and the physical requirements for any failure mechanism. If strain-rate is a key factor controlling the variable distribution of seismicity in slabs, then the seismic strain-rate should reflect the actual strain-rate in the slab (just as seismicity reflects strain-rate within the plates at the surface). In this case, multiple failure mechanisms for deep earthquakes are possible, but all require sufficient strain accumulation, and therefore earthquakes are limited to cold *and* high strain-rate regions. Alternatively, if the strain-rate is uniform within the slab, then the strain-rate is not an important factor, and in this case, some other factor controlling appropriate conditions for the various failure mechanisms will determine the seismicity pattern. Because it is not possible to directly measure the strain-rate in slabs, I use numerical simulations to estimate the strain-rate distribution.

2D Dynamic Models of Subduction

The strain-rate within the slab depends both on the rheology used in the models and the effect of phase transitions on the time-dependent evolution of the slab. For the strongly temperature-dependent viscosity of olivine, the slab rheology is primarily determined by the yield strength and maximum viscosity allowed in the models. This means that the slab interior is stiff and resists

internal deformation. Therefore, the stresses caused by sinking of the slab are primarily accommodated by flow in the surrounding mantle. However, during episodes of slab folding yielding within the slab leads to regions of localized internal deformation with higher strain-rate.

Model 1 shows the evolution of an 80 my old slab in which no phase changes are included (Figure 3A; Movie S1). At the start of subduction the stress due to negative slab buoyancy is small and the main area of deformation is the bending region at the outer rise, which exhibits a classic hour-glass shaped yielding region (Fig 3A.a). As the slab lengthens, it sinks rapidly through the upper mantle and experiences high strain-rates throughout; the slab sinks faster than the trailing plate and stretches due to low viscous resistance from the surrounding mantle (Fig 3A.b). Once the slab reaches the viscosity jump at the top of the lower mantle, it slows down as the buoyancy of the slab becomes partially supported by higher viscosity in the lower mantle. At the same time the internal strain-rate decreases dramatically and the effective viscosity increases (Fig 3A.c). Subsequently, the slab dip shallows slightly, but there is otherwise little change to the slab shape or sinking rate for the remainder of the simulation (Fig 3A.d).

In Model 2, the evolution of the slab is quite different owing to the effect of the phase transitions (Figure 3B; Movie S2). The evolution of the slab is similar to Model 1 until the slab starts to interact with the more viscous lower mantle. At this point, there is a strongly time-dependent strain-rate pattern associated with the bending and buckling of the slab. As shown previously, the density anomalies associated with the phase transitions cause folding and buckling of the slab as well as forward and retrograde motion of the trench (*30, 34*). High strain-rate regions form in regions of bending with an hour-glass pattern characteristic of bending with a neutral plane. In addition, there is a region of high strain-rate at 550–650 km depth, which occurs with or without slab bending. This high strain-rate region occurs between the garnet to ilmenite (elevated) and

garnet to brigmanite (depressed) transitions in the harzburgite layer.

For Model 2, the maximum strain-rate occurring below a temperature limit (e.g., 1000°C) is plotted as a function of depth (Figure 3B.e–h). The depth profiles show high strain-rates at shallow depths (< 100 km) corresponding the high rates of deformation along the slab surface and in the bending region at the trench. Below this depth, the strain-rate magnitude generally decreases with a minimum near 300 km. In the transition zone the shape of the profile is strongly time-variable as the slab folds and buckles. During significant bending events the maximum strain-rate does not depend strongly on temperature, while at other times the maximum strain-rate is higher at temperatures of 900–1000°C. The depth and width of strain-rate peaks, as well as the number of strain-rate peaks, changes in time. Note also, that the strain-rate drops sharply crossing into the higher viscosity lower mantle. These strain-rate profiles have similar characteristics to the strain-rate profiles calculated from observed seismicity. It is these similarities in strain-rate between the long-term subduction models and the observations that argue in favor of strain-rate as an important environmental variable determining the distribution of deep earthquakes.

Model 3 is the same as Model 2 except that the initial subducting plate age is younger (40 my). Here the evolution of the slab and strain-rate pattern is similar to Model 2 exhibiting peaks in strain-rate during bending and folding (Figure 3C; Movie S3). However, because the slab is younger it is also warmer with the 700–800°C isotherms restricted to depths less than 400 km and periods of time when the 1000°C contour does not extend past 660 km or becomes broken. Also, because the slab is warmer it has a smaller integrated strength and it deforms at higher strain-rates overall. Note that in the deeper, warmer regions of the slab, the stress levels are lower because the slab is not deforming at the yield stress, and therefore, despite the higher strain-rates, seismicity might not be expected to occur in these regions.

In all three models, the stress orientations indicate that the slab exhibits down-dip compression (DDC) along the top/central part of the slab ($\sim$ 200–660 km), except in regions of folding, consistent with earlier studies (*21, 35*). In the folding regions, the location of DDC shifts to the high strain-rate region on the under-side of the slab, and the stretching orientation is parallel to the folded slab surface. This suggests that the envelope of seismicity defining the location of deep slabs may in fact shift from the top of the slab to the bottom of the slab depending on the orientation of folding at the depth.

Comparison of Observations and Models

The models show a dynamic view of continuously changing slab shape and peaks in strain-rate. For the Earth, however, we have only a single snap-shot in time. One way around this is to recognize that for 3D slabs, their shape evolves in time and in space, so that adjacent profiles capture the time evolution of the changing shape. This is a commonly used space for time substitution from structural geology. Using this approach, comparison shows that both the observations and the models exhibit peaks in strain-rate of variable magnitude, depth and width. In the models, peaks follow regions of bending in time (Figure 4), while in observations, there are many examples of the depth and shape of a peaks systematically changing along strike (Figure 2 and S3), and of seismicity following lines of high-curvature along-strike (*27*). In the models, there are times where strain-rate is low throughout much of the slab, just as there are profiles in the observations that have very low seismicity adjacent to regions with higher seismicity (e.g., Japan).

In addition to the time-variable evolution of the strain-rate profiles, there are two more general characteristics of the strain-rate profiles to explain. First, note that in the models the strain-rate

decreases to a minimum value beneath 660 km, for all times, regardless of the shape of the slab at this depth (Figures 3 and 4). This drop in strain-rate within the slab is caused by the increased viscous support provided by the higher viscosity of the lower mantle. This higher viscosity slows down the overall rate of deformation of the slab (by a factor of 100) and the surrounding mantle. The increase in viscous support by the surrounding mantle also means that much less stress must be supported by the slab itself. And, the slab is no longer bending and buckling, but rather sinks passively (< 1 cm/yr) into the lower mantle. This suggests that the cessation of seismicity at 660 km depth could be controlled by the change in rheology, which causes an overall lower strain-rate in the slab and surrounding mantle. However, it is also true that transformational faulting from metastable olivine also shuts off beyond 660 km because the transformation to bridgmanite plus ferropericlase is endothermic (*36*).

Second, there is a peak in strain-rate just below 600 km that persists even when there is not significant bending of the slab at this depth (Figure 4). Figure 5 shows that this peak occurs at the garnet-to-Bridgmanite transition in the harzburgite layer, which lies between the elevated garnet-ilmenite phase transition (g-i) and the depressed ilmenite-to-Bridgmanite (i-B) and Ringwoodite-to-Bridgmanite plus ferropericlase (R-B+f) phase transitions. The region between these two phase transitions is subject to net compression caused by the negative buoyancy above (g-i) and positive buoyancy below (i-B and R-B+f). This compression causes a higher localized stress, which due to yielding leads to a reduction in viscosity and higher strain-rate. This result suggests that accurately accounting for the phase transitions in both the pyroxene and olivine components of the slab, as is done in these simulations, is essential for fully accounting for the buoyancy forces affecting the overall deformation of the slab and causing deep slab seismicity.

Because the numerical simulations are fully dynamic, the evolution of subduction rates and

trench motion, and thus slab shape are determined by the time-evolving balance of forces. Therefore, the models do not correspond to any particular subduction zone on Earth. However, because the time steps in the models correspond to thousands of years, and the strain-rates are determined by the instantaneous balance of forces and the rheology, snap-shots from the models with similar geometry can be compared to observed profiles.

First, is a comparison between a model snap-shot and a profile from Chile (Figure 6A). The Chile slab has a fairly planar shape below the shallow flat-slab segment (*28*) and is thought to be sinking directly into the lower mantle (*37*), similar to the model snap-shot. Both the model and observations exhibit low strain-rates above the transition zone with a peak around 600 km associated with the phase transitions at this depth. Similar profiles are also seen in Peru and portions of Java-Sumatra (see Figure S3F and G).

Second, is a comparison for the Mariana slab (Figure 6B). The model snap-shot shows an overturned slab with high strain-rate regions between 350–500 km and a second peak associated with the garnet-ilmenite transitions near 600 km. While typical profiles of slabs do not exhibit this overturned shape, sections of the Mariana and Java-Sumatra slabs are clearly overturned (see Figure S2). The distance from the western-most limit of the slab and the slab tip at 700 km is about 250 km in the model and about 200 km in the observations. The high strain-rate region in the model at 350–500 km depth corresponds to a cluster of events in the Marianas slab with no seismicity above or below this bending region (except for one very deep event). However, note that the high stain-rate region at 350–500 km depth in the model occurs on the bottom of the plate with down-dip compression, while the deeper strain-rate peak occurs across the slab width. If the location of deep earthquakes is controlled by strain-rate, then these results require that some events initiate in the lithospheric portion of the plate, rather than the crust or harzburgite layers: an important

observation for determining which failure mechanisms may be active in different locations in the slab.

Third, is a comparison between a model snap shot and a profile from the Bonin slab (Figure 6C). The profile is from the region of the slab between the shallow-dipping, planar slab to the north in Japan, and the steeply-dipping, curved slab to the south in the Marianas (see map in Fig S2E). Note that the shape of the profile seen here exists over 200–250 km along strike. The seismicity indicates that the slab flattens to the west just below 500 km depth (the 1982 Mw 6.7 outboard event is noted). However, there is also an event at 680 km depth behind (east) of the shallower seismicity and separated by a gap. This deep earthquake is the 2015 Mw 7.8 Ogasawara (Bonin) Islands event (*38*). One possibility to explain the change in geometry across such a narrow region is a tear in the slab (*39*). A second possibility is that the slab is folded (*38*), as shown in the model snap-shot. Note that in this snap-shot there is a region of high strain-rate in the outboard, top portion of the fold, but the strain-rate in the bottom of the fold is low. The fold in the model snap-shot is also broader than the fold needed to explain the earthquakes, indicating that more intense weakening of the slab is required during folding.

Discussion

The numerical models show that high strain-rate regions occur where the slab is bending or folding, and locally between phase transitions with opposite Clapeyron slopes. Both the modeled strain-rate and observed strain-rate profiles exhibit: 1) peaks of variable magnitude, depth and width, 2) regions of very low strain-rate (gaps in seismicity), and 3) a sharp drop-off in strain-rate below 660 km. The similarity in the strain-rate profiles from the models and from the seismicity show

that seismic strain-rate directly reflects the actual strain-rate of the slab. Therefore, the spatial variation in deep earthquake seismicity is determined by the spatial pattern in strain-rate within strong, deforming slabs.

This conclusion requires that the slab rheology is such that the slab is viscously strong (strong temperature-dependent viscosity) and that it can yield in response to localized higher stresses. If a lower yield stress (or lower maximum viscosity) were used, the whole slab would deform at a higher rate. However, in these models, a lower yield stress causes the slab to break-off due the added negative buoyancy from the phase transitions (*34*) compared to other models that use a lower yield stress (e.g., (*40*)). Also, a lower yield stress may not be consistent with the large stress drops (up to 100's of MPa) estimated for some deep earthquakes (*9, 41*) or the differential stress at which low temperature plasticity would occur in cold slabs (*25*).

The yield stress, or use of a strong power-law exponent (*31*), is an approximation to low temperature plasticity (i.e., Peierls creep). At shallow depth, the yield stress is also used to approximate brittle failure through frictional processes (i.e., Byerlee's law). A better approximation of the low temperature plasticity may be achieved using a temperature-dependent power-law exponent (*42*), and would likely lead to overall higher strain-rates in the cold interior of the slab, but would still exhibit peaks in strain-rate in regions of bending or folding. Similarly, including the effects of elasticity with a visco-elastic rheology would also decrease the magnitude of stress in the slab, and can result in a lower apparent slab viscosity (*43*). It is also important to note that slab temperature remains an important factor for deep seismicity. Young and slowly sinking slabs will not have deep seismicity because they are too warm and therefore deform through diffusion and dislocation creep. In this case, the stress in the slab is relaxed viscously.

The idea that strain-rate is an important factor in understanding deep earthquakes is not new,

but it has been largely ignored or forgotten in the literature relating potential failure mechanisms to the physical state of the slab. The mechanism of shear instability explicitly relies on having a high enough strain-rate (and stress) to cause shear heating (*3*) however localized grain-size reduction is likely necessary to reach sufficient strain-rates for this mechanism to be viable (*5*). Transformational faulting of olivine also requires a sufficient strain-rate and the strain-rate affects the window of temperatures at which this mechanism occurs in the laboratory (see Figure 4 in (*6*)). However, while many previous models explore the state of stress in the slab (e.g., (*21, 22, 44*)) and evolution of an MO wedge they do not also assess the strain-rate requirements (e.g., (*18*)). Finally, the correspondence of high strain-rate with regions of bending and buckling in the models also agrees with the observation that earthquakes appear to align with regions of high slab curvature (*27*) and the higher rates of seismicity in strongly-deformed slabs (e.g., Tonga, (*45*)).

While several studies have used seismic strain-rate as a minimum constraint on the slab strain-rate (and maximum viscosity) required in dynamic models of subduction (e.g., (*40, 46*)), these models have not considered the spatial variability in strain-rate and how this may be related to the rheology of the slab. In contrast, many past studies of subduction have employed simplified rheologies and inherently weak slabs (see (*32*) and review by (*47*)). While such weak slab models may meet the minimum average strain-rate requirement, they are inconsistent with laboratory constraints on rheology, the requirement that slabs be strong enough to store stresses that are released seismically (not through viscous flow), and the large observed stress drops for some deep earthquakes.

While the models presented here provide compelling evidence that strain-rate is an important factor, together with the thermal structure, determining the distribution of deep earthquakes, there are limitations that must be explored in future models, including low temperature plasticity,

elasticity, tectonic overpressure from phase transitions, inclusion of a metastable olivine wedge, compressibility, and 2D geometry (this list is addressed in the Supplementary Material). Systematically addressing these limitations will surely impact the details of the slab deformation, and the magnitudes of the strain-rates and stresses, but are unlikely to effect the primary conclusions presented here because the slabs will still bend and buckle with spatially and temporally variable strain-rate. To further link the dynamical models to possible failure mechanism, running identical subduction models, both with and without metastable olivine, for a range of thermal parameters, would facilitate analyzing how stress magnitudes and orientations are related to portions of the slab that have appropriate temperature and strain-rate conditions for the possible deep earthquake failure mechanisms.

Incorporation of better approximation of low temperature plasticity, followed by elasticity and compressibility should be primary targets for further study because this will allow more direct comparison between the strain-rate and stress states in the models and the conditions required for each deep earthquake failure mechanism. It is important to note that Farrington et al., (*43*) show that the mode of subduction and slab morphology are not affected by inclusion of elasticity in 3D models of free subduction, therefore the distribution of high strain-rate regions associated with bending in the slab would also not be affected. However, the location of the maximum stress (and its magnitude) and the stress orientations within the bending region is shifted because the stress and strain-rate are not generally co-axial in viscoelastic materials. It is for this reason that the stress orientations from the slab models have not been analyzed in detail or compared directly with moment tensor solutions.

Progress in understanding the triggering mechanisms for deep earthquakes has been slowed by an insufficient physical framework to adequately demonstrate or refute the viability of proposed

failure mechanisms. Taking into account the added constraint of strain-rate should help to resolve which of these mechanisms are active in the subducting lithosphere, with the possibility that multiple mechanisms may be required to explain the variability within and between slabs of varying age and state of deformation. Considering the rate of deformation and the process through which strain accumulates in the slab more explicitly, may also foster re-evaluation of seismic observations related to rupture behavior (moment release, rupture time), b-values, aftershock occurrence and stress drop and how these are related to different triggering mechanisms. For example, considering the detailed orientations of stress and strain in bending regions in conjunction with a physical model of the failure mechanism may help to explain the preference for near-horizontal failure planes for deep earthquakes (*48*) and the large depths (near 660 km) for the largest deep earthquakes (*11*). In addition, it is possible that the observed correlation of b-values with thermal parameter (*15*) may also be related to the strain-rate of the slab. This is because 1) faster sinking slabs are expected to undergo more internal deformation to accommodate the viscous resistance to sinking into the lower mantle, and 2) the correlation between b-value and thermal parameter is primarily controlled by the sinking rate. This is why, for example Tonga has a higher thermal parameter than Japan, even though the subducting plate in Tonga is younger than in Japan. Finally, the spatially-variable strain-rate can be used to further constrain the appropriate rheology for the lithosphere by providing a direct link between the short time-scale phenomena of strain release through earthquakes and the long-term deformation of slabs.

Conclusions

The spatial distribution of deep earthquakes exhibits significant variability between different subduction zones and along-strike within individual subduction zones. Existing explanations for deep earthquakes assume that the distribution of seismicity is primarily determined by whether the appropriate thermal conditions exist in the slab for a variety of special triggering mechanisms. Here I have shown that the strain-rate distribution from simulations of strong, but deforming slabs has the same variability as the observed strain-rate: peaks in strain-rate at variable depths, regions of low strain-rate, and a sharp drop-off in strain-rate at 660 km. The results presented here can not distinguish between possible failure mechanisms for deep earthquakes. However, they do suggest a new approach for testing these mechanism that would combine the thermal and strain-rate constraints with appropriate rheological models. With such models it may be possible to more directly link the required conditions (e.g., pressure, temperature, strain-rate) for viable failure mechanisms with seismic observations of deep earthquakes (e.g., stress drop, radiation efficiency, b-values) and to better constrain the rheology of the lithosphere and mantle.

Methods

I compare the time-dependent evolution of deformation within subducting lithosphere to the seismically-accommodated strain-rate observed in present-day slabs. For the numerical simulations I use the second invariant of the strain-rate tensor to quantify the magnitude of the strain-rate. The seismic strain-rate is calculated following the analysis of Bevis (*49*). While these are both measuring deformation within the slab, the seismic strain-rate is by definition the deformation that is not accommodated by viscous deformation. Therefore, the spatial pattern (depth-dependence) of the strain-rates is compared, but not the magnitudes.

Dynamic Subduction Models

The subduction models are fully described in Billen and Arredondo (*30*). The time-dependent evolution of the sinking lithosphere (slab) is modeled in a two-dimensional (2D) slice of a spherical shell extending from the surface to the core-mantle boundary and 61° in longitude (Figure S1). Simulations are run using the CitcomS finite element code (*50*). CitcomS solves the conservation equations for mass, momentum and energy using the extended Boussinesq approximation, which assumes incompressibility, but includes an initial adiabatic gradient, shear heating and latent heat from phase transitions (*51*). The model set-up allows for fully dynamic simulations in which only buoyancy forces drive subduction, plate and trench motions (free subduction): all boundaries have a zero normal velocity and no tangential stress (free-slip). To allow the plates to move freely toward or away from the sidewalls, we imposed a boxed region at the trailing end of both plates that has a fixed thermal profile and low viscosity. Subduction is initiated with a proto-slab extending to a depth of 200 km.

Key features of the model set-up include (Figure S1): 1) a layered compositional density structure for the subducting and overriding plates, 2) a composite visco-plastic rheology based on laboratory experiments for olivine, and 3) compositionally-dependent phase transitions. In addition, the basaltic crustal layer is modeled as a weak layer (maximum viscosity of 10^{20} Pa s), which allows the subducting plate to slide past the overriding plate. The maximum viscosity reverts to the global maximum of 10^{24} Pa s as the basalt transitions to eclogite (at 80–100 km). All of the parameters for the composite viscosity and phase transitions are documented in Billen and Arredondo (*30*).

Seismic Strain-rate Calculation

The strain-rate associated with seismicity in the subducted lithosphere is calculated following Bevis (*49*). This calculation relates the moment released within in a volume of the slab to the down-dip strain-rate,

$$\dot{\epsilon}_s = \frac{\sum_T M_o}{2\mu V T} \tag{1}$$

where $\sum_T M_o$ is the total moment released within a volume, V, during a time period, T, and μ is the rigidity. For this calculation a volume of slab material, $V = WHL$ is considered, where W is trench parallel width, H is slab thickness, and L is the down-dip slab length. Equation 1 results from considering that the slip in each event, D, is related to the seismic moment by $M_o = \mu A D$, where the fault area is A. The average slip accumulated within a time period, T, is

$$\hat{D} = \sum_T M_o / \mu W H, \tag{2}$$

where the average fault area is taken as $A = WH$. Assuming this slip accommodates down-dip deformation, the change in down-dip length is

$$\delta = \sum_T M_o / 2\mu W H. \tag{3}$$

The down-dip strain is then given by $\epsilon = \delta/L$ and the strain-rate by $\dot{\epsilon} = \delta/LT$.

The strain-rate is calculated along evenly spaced trench-perpendicular profiles located every 200 km (W) along the trench, in 10 km depth intervals (dz), assuming a constant seismogenic thickness of 80 km (H). For Tonga, I use $W = 100$ km because the seismicity rate is much higher than in other subduction zones. A value of 60 GPa is used for the rigidity (*49*). In PREM the rigidity increases by a factor of 2 with depth in the upper mantle. However, at the same time the seismogenic width is also expected to decrease with depth as the slab warms. Therefore, these to changes will largely cancel out. In addition, the changes in strain-rate of interest vary by 10–100×. Therefore, for simplicity, I use a constant value for rigidity and seismogenic thickness. The down-dip length of the slab within each depth bin depends on the average dip of the slab within each depth bin, α, as $L = dz/\sin(\alpha)$. Using the Slab 2.0 geometry model (*28*), the average slab dip is calculated from all points in the depth bin and located within 100 km ($0.5W$) of the profile.

Earthquake data for a 50 year time period (1964–2014) are downloaded from the ISC-EHB catalog for depths of 100–700 km and magnitudes of 4.0 and greater (*52*). A map and the earthquake profiles for each region are shown in Figures S2–S9. For this time period all the earthquakes have been relocated using the EHB algorithm, which provides better earthquake locations, and in particular better depth estimates than previous ISC determinations (*53*). Moment magnitudes are used when available, otherwise body-wave magnitude is converted to moment magnitude using the relationship $M_w = 0.85m_b + 1.03$ (*54*). The moment for each event is then given by $M_o = 10^{1.5(10.7+Mw)}$ (note this gives the moment in dyne-cm; 1 N-m is 10^7 dyne-cm). Finally, for each subduction zone, the regional strain-rate as a function depth is determined by summing the profiles. Plots of the seismicity rate and strain-rate as a function of depth along each of the profiles are included in the Supplementary Materials (Figure S3A–H).

For any study using seismicity to constrain rates of deformation one must be aware that the relatively short (50 years) duration over which data is available may not capture seismicity that occurs on a longer time-scale. In particular, since the rate of seismicity in deep slabs is quite low compared to rates along plate boundaries at the surface, apparent gaps in seismicity may be filled in by longer observation times. Similarly, an isolated, but rare, large events can result in an apparent spike in strain-rate. For example, the M 8.3 Okhotsk event in the Kuriles is the largest deep earthquake recorded and appears as a strain-rate spike at 600 km depth in Figure 1F, and Figure S3C (profile 8).

References

1. B. R. Hacker, G. A. Abers, S. M. Peacock, Subduction factory 1: Theoretical mineralogy, density, seismic wave speeds and H_2O contents. *Journal of Geophysical Research* **108** (2003).

2. C. G. Barcheck, D. A. Wiens, P. E. van Keken, B. R. Hacker, The relationship of intermediate- and deep-focus seismicity to the hydration and dehydration of subducting slabs. *Earth and Planetary Science letters* **349-350**, 153-160 (2012).

3. M. Ogawa, Shear instability in a viscoelastic material as the cause of deep focus earthquakes. *Journal of Geophysical Research* **92**, 13801–13810 (1987).

4. T. Ohuchi, X. Lei, H. Ohfuji, Y. Higo, Y. Tange, T. Sakai, K. Fujino, T. Irifune, Intermediate-depth earthquakes linked to localized heating in dunite and harzburgite. *Nature Geoscience* **10**, 771-776 (2017).

5. M. Thielmann, Grain size assisted thermal runaway as a nucleation mechanism for continental mantle earthquakes: Impact of complex rheologies. *Tectonophysics* **746**, 611-623 (2018).

6. P. C. Burnley, H. W. Green II, D. J. Prior, Faulting associated with the olivine to spinel transformations in Mg_2GeO_4 and its implications for deep-focus earthquakes. *Journal of Geophysical Research* **96**, 425–443 (1991).

7. A. Schubnel, F. Brunet, N. Hilairet, J. Gasc, Y. Wang, H. W. Green II, Deep-focus earthquake analogs recorded at high pressure and temperature in the laboratory. *Science* **341**, 1377-1380 (2013).

8. M. Nishi, T. Kubo, H. Ohfuji, T. Kato, Y. Nishihara, T. Irifune, Slow Si–Al interdiffusion in garnet and stagnation of subducting slabs. *Earth and Planetary Science Letters* **361**, 44-49 (2013).

9. H. Houston, *Treatise on Geophysics*, G. Schubert, ed. (Elsevier Ltd, Oxford, U.K., 2007).

10. C. Frohlich, *Deep Earthquakes* (Cambridge University Press, 2006).

11. Z. Zhan, Mechanisms and implications of deep earthquakes. *Annual Reviews of Earth and Planetary Sciences* **48**, 1-28 (2020).

12. M. Vallée, Source time function properties indicate a strain drop independent of earthquake depth and magnitude. *Nature Communications* **4**, 1-6 (2013).

13. H. Kanamori, D. L. Anderson, T. H. Heaton, Frictional melting during the rupture of the 1994 Bolivian earthquake. *Science* **279**, 839-842 (1998).

14. B. Harte, Diamond formation in the deep mantle: the record of mineral inclusions and their distribution in relation to mantle dehydration zones. *Mineralogical Magazine* **74**, 189–215 (2010).

15. Z. Zhan, Gutenberg–Richter law for deep earthquakes revisited: A dual-mechanism hypothesis. *Earth and Planetary Science Letters* **461**, 1-7 (2017).

16. P. B. Kelemen, G. Hirth, A periodic shear-heating mechanism for intermediate-depth earthquakes in the mantle. *Nature* **446**, 787-790 (2007).

17. S. H. Kirby, W. B. Durham, L. A. Stern, Mantle phase changes and deep-earthquake faulting in subducting lithosphere. *Science* **252**, 216-225 (1991).

18. M. Tetzlaff, H. Schmeling, Time-dependent interaction between subduction dynamics and phase transition kinetics. *Geophysical Journal International* **178**, 826-844 (2009).

19. F. Marton, T. J. Shankland, D. C. Rubie, Y. Xu, Effects of variable thermal conductivity on the mineralogy of subducting slabs and implications for mechanisms of deep earthquakes. *Physics of the Earth and Planetary Interiors* **149**, 53-64 (2005).

20. S. Yoshioka, Y. Torii, M. R. Riedel, Impact of phase change kinetics on the Mariana slab within the framework of 2-d mantle convection. *Physics of Earth and Planetary Interiors* **240**, 70-81 (2015).

21. M. S. Vassiliou, B. H. Hager, A. Raefsky, The distribution of earthquakes with depth and stress in subducting slabs. *Journal of Geodynamics* **1**, 11-28 (1984).

22. A. Guest, G. Schubert, C. W. Gable, Stress field in subducting lithosphere and comparison with deep earthquakes in Tonga. *Journal of Geophysical Research* **108**, 2288 (2003).

23. L. Burlini, D. Bruhn, *High strain zones: Structure and Physical Properties*, D. Bruhn, L. Burlini, eds. (Geological Society, London, 2005), vol. 245 of *Special Publications*, pp. 1–24.

24. R. Wortel, Seismicity and rheology of subducted slabs. *Nature* **296**, 553-556 (1982).

25. S. Mei, A. M. Suzuki, D. L. Kohlstedt, N. A. Nixon, W. B. Durham, Experimental constraints on the strength of the lithospheric mantle. *Journal of Geophysical Research* **115** (2010).

26. J. Brodholt, S. Stein, Rheological control of Wadati-Benioff zone seismicity. *Geophysical Research Letters* **15**, 1081–1084 (1988).

27. R. Myhill, Slab buckling and its effect on the distributions and focal mechanisms of deep-focus earthquakes. *Geophysical Journal International* **192**, 837-853 (2013).

28. G. P. Hayes, G. L. Moore, D. E. Portner, M. Hearne, H. Flamme, M. Furtney, G. M. Smoczyk, Slab2, a comprehensive subduction zone geometry model. *Science* **362**, 58-61 (2018).

29. H. Cížková, C. Bina, Effects of mantle and subduction-interface rheologies on slab stagnation and trench rollback. *Earth and Planetary Science Letters* **379**, 95-103 (2013).

30. M. I. Billen, K. M. Arredondo, Decoupling of plate-asthenosphere motion caused by non-linear viscosity during slab folding in the transition zone. *Physics of the Earth and Planetary Interiors* **281**, 17-30 (2018).

31. F. Garel, S. Goes, D. R. Davies, J. H. Davies, S. C. Kramer, C. R. Wilson, Interaction of subducted slabs with the mantle transition-zone: A regime diagram from 2-D thermo-mechanical models with a mobile trench and an overriding plate. *Geochemistry, Geophysics, Geosystems* **15**, 1739–1765 (2014).

32. W. C. Tao, R. J. O'Connell, Deformation of a weak subducted slab and variation of seismicity with depth. *Nature* **361**, 626-628 (1993).

33. S.-I. Karato, M. R. Riedel, D. A. Yuen, Rheological structure and deformation of subducted slabs in the mantle transition zone: implications for mantle circulation and deep earthquakes. *Physics of the Earth and Planetary Interiors* **127**, 83-108 (2001).

34. K. M. Arredondo, M. I. Billen, Coupled effects of phase transitions and rheology in 2D dynamical models of subduction. *Journal of Geophysical Research* **122**, 5813-5830 (2017).

35. L. A. Alpert, T. W. Becker, I. W. Bailey, Global slab deformation and centroid moment tensor constraints on viscosity. *Geochemistry, Geophysics and Geosystems (G^3)* **11**, Q12006 (2010).

36. H. W. Green II, H. Houston, The mechanics of deep earthquakes. *Annual Reviews of Earth and Planetary Science* **23**, 169-213 (1995).

37. J. Zahradník, H. Cížková, C. R. Bina, E. Sokos, J. Janský, H. Tavera, J. Carvalho, A recent deep earthquake doublet in light of long-term evolution of Nazca subduction. *Nature Scientific Reports* **7**, 1-11 (2017).

38. L. Ye, T. Lay, Z. Zhan, H. Kanamori, J.-L. Hao, The isolated ∼680 km deep 30 May 2015 M_w 7.9 Ogasawara (Bonin) Islands earthquake. *Earth and Planetary Science Letters* **433**, 169–179 (2016).

39. H. Zhang, F. Wang, R. Myhill, H. Guo, Slab morphology and deformation beneath izu-bonin. *Nature Communications* **10**, 1-8 (2019).

40. L. Alisic, M. Gurnis, G. Stadler, C. Burstedde, L. C. Wilcox, O. Ghattas, Slab stress and strain rate constraining global mantle flow. *Geophysical Research Letters* **32** (2010).

41. T. B. Andersen, K. Mair, H. Austrheim, Y. Y. Podladchikov, J. C. Vrijmoed, Stress release in exhumed intermediate and deep earthquakes determined from ultramafic pseudotachylyte. *Geology* **36**, 995-998 (2008).

42. M. Kameyama, D. A. Yuen, S.-I. Karato, Thermal-mechanical effects of low-temperature plasticity (the Peierls mechanism) on the deformation of a visco-elastic shear zone. *Earth and Planet. Sci. Lett.* **168**, 159-172 (1999).

43. R. J. Farrington, L.-N. Moresi, F. A. Capitanio, The role of viscoelasticity in subducting plates. *Geochemistry Geophysics Geosystems* **15**, 4191-4304 (2014).

44. C. R. Bina, Patterns of deep seismicity reflect buoyancy stresses due to phase transitions. *Geophysical Research Letters* **24**, 3301-3304 (1997).

45. S. Richards, R. Holm, G. Barber, When slabs collide: A tectonic assessment of deep earthquakes in the Tonga-Vanuatu region. *Geology* **39**, 787-790 (2011).

46. M. I. Billen, M. Gurnis, M. Simons, Multiscale dynamic models of the Tonga-Kermadec subduction zone. *Geophysical Journal International* **153**, 359-388 (2003).

47. M. I. Billen, Modeling the dynamics of subducting slabs. *Annual Reviews of Earth and Planetary Science* **36**, 325-356 (2008).

48. L. M. Warren, A. N. Hughes, P. G. Silver, Earthquake mechanics and deformation in the Tonga-Kermadec subduction zone from fault-plane orientations of intermediate- and deep-focus earthquakes. *Journal of Geophysical Research* **112** (2007).

49. M. Bevis, Seismic slip and down-dip strain rates in Wadati-Benioff Zones. *Science* **240**, 1317-1319 (1988).

50. S. Zhong, M. T. Zuber, L. Moresi, M. Gurnis, Role of temperature-dependent viscosity and surface plates in spherical shell models of mantle convection. *J. of Geophys. Res.* **105**, 11063-11082 (2000).

51. U. R. Christensen, D. A. Yuen, Layered convection induced by phase transitions. *Journal of Geophysical Research* **90**, 10291-10300 (1985).

52. ISC-EHB, The ISC-EHB Bulletin 1960–2014, www.isc.ac.uk/isc-ehb/, last accessed on November 26 (2018).

53. E. R. Engdahl, R. van der Hilst, R. Buland, Global teleseismic earthquake relocation with improved travel times and procedures for depth determination. *Bulletin of the Seismological Society of America* **88**, 722-743 (1998).

54. E. M. Scordilis, Empirical global relations converting M_S and m_b to moment magnitude. *Journal of Seismology* **10**, 225-236 (2006).

55. K. Arredondo, M. I. Billen, The effects of phase transitions and compositional layering in two-dimensional kinematic models of subduction. *Journal of Geodynamics* **100**, 159-174 (2016).

56. B.-D. So, D. A. Yuen, Generation of tectonic over-pressure inside subducting oceanic lithosphere involving phase-loop of olivine–wadsleyite transition. *Earth and Planetary Science Letters* **413** (2015).

57. R. Gassmöller, J. Dannberg, W. Bangerth, T. Heister, R. Myhill, Capturing dynamic effects of compressible mantle convection: New formulations and numerical methods (DI33C-0049), Presented at the 2019 Fall Meeting, AGU, San Francisco, CA 9-13 Dec. (2019).

58. J. P. Devaux, L. Fleitout, G. Schubert, C. Anderson, Stresses in a subducting slab in the presence of a metastable olivine wedge. *Journal of Geophysical Research* **105**, 13365-13373 (2000).

59. CMT-Catalog, Global centroid moment tensor catalog, www.globalcmt.org, last accessed on December 1 (2018).

60. G. Ekström, M. Nettles, A. M. Dziewonski, The global CMT project 2004-2010: Centroid-moment tensors for 13,017 earthquakes. *Physics of the Earth and Planetary Interiors* **200-201** (2012).

Acknowledgements. I would like to thank two anonymous reviewers and Zhongwen Zhan for their constructive comments. An archive for the numerical models is included with previous publications cited. All earthquake data are publicly available at the websites cited. Figures were made with the GMT plotting software. The Computational Initiative for Geodynamics (CIG) supports the CitcomS software used for the numerical simulations. The author declares that she has no competing interests. **Funding:** This project was supported by a fellowship of the Alexander von Humbolt Foundation. The numerical simulations research was funded by the National Science

Foundation, award #1246864.

Figures

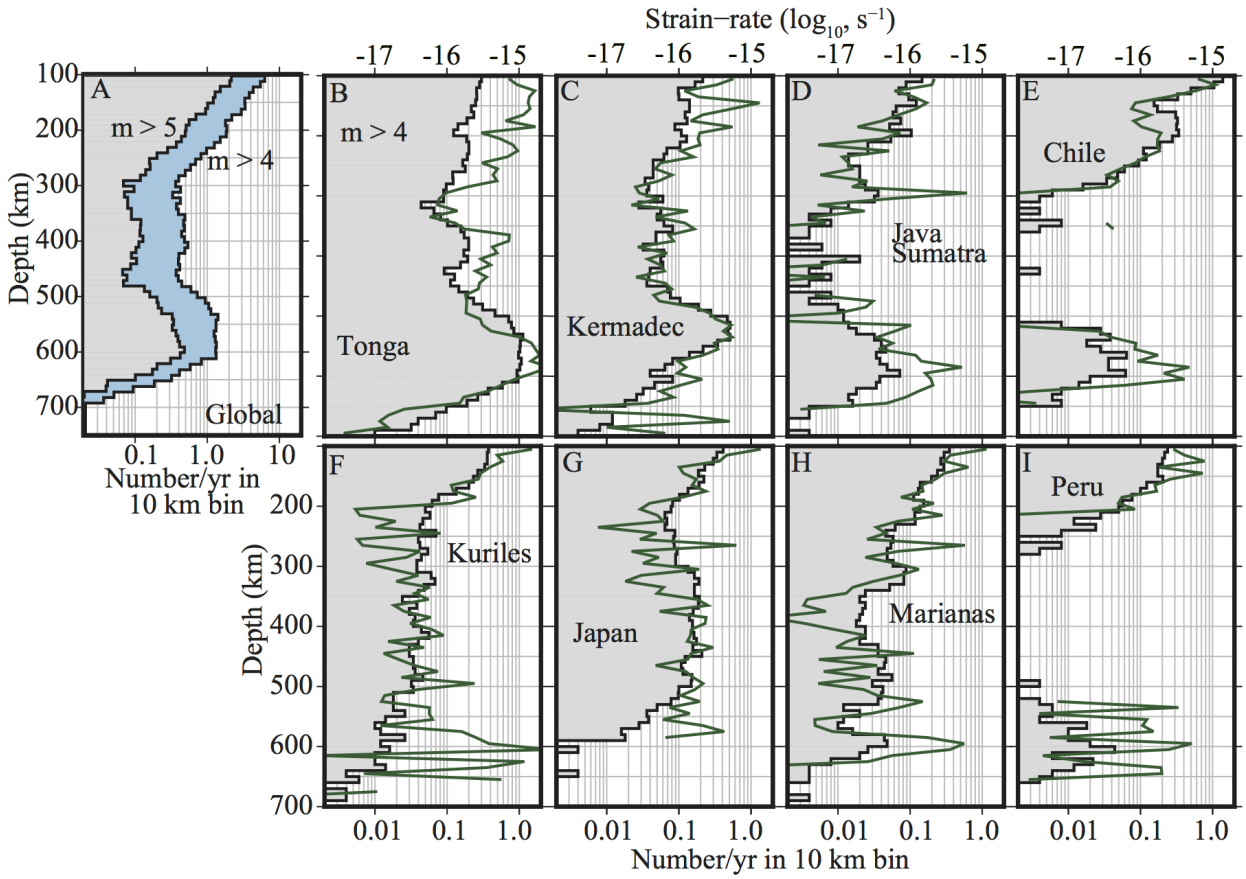

Figure 1: Subduction zones exhibit strong variability of seismicity and strain-rate in depth. **A**. Global seismicity in subduction zones for earthquakes greater than 100 km depth for $M_w > 4$ (blue) and $M_w > 5$ (gray) for the period 1964–2014 from the EHB-ISC Catalog (*52*). **B–I**. Regional seismicity rate and strain-rate versus depth. Tonga (B), Kermadec (C) and Java-Sumatra (D) all have regional seismicity depth profiles that mimic the global profile in A. The Kuriles (F), Japan (G) and Marianas (H) do not exhibit the characteristic increase in seismicity rate within the transition zone (400–660 km). Chile (E) and Peru (I) have a distinct lack of seismicity from 300–500 km, but do have earthquakes in the transition zone from 500–660 km.

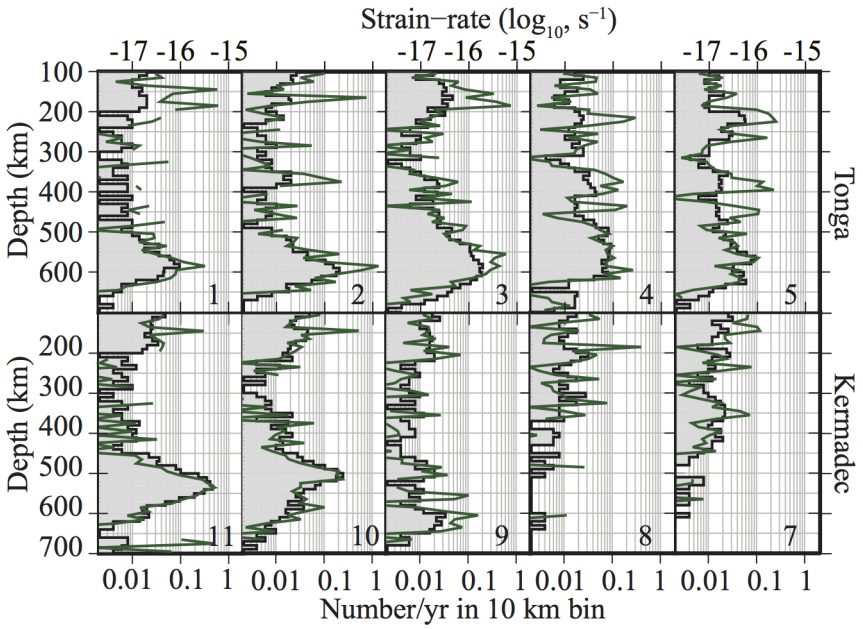

Figure 2: Seismicity and strain-rate exhibit continuous changes in peak depth and width along adjacent profiles. Examples from the Tonga (1–5) and Kermadec (7–11) slabs. From profiles 1 through 5, there is a continuous change in the depth and width of the transition zone peak and the emergence of a narrow strain-rate peak at 400 km depth. From profile 11 to 7, the transition zone peak disappears, being replaced by two smaller peaks, and then a shift to a broad peak centered at 400 km depth. Locations of profiles are shown in Figures S2A–B.

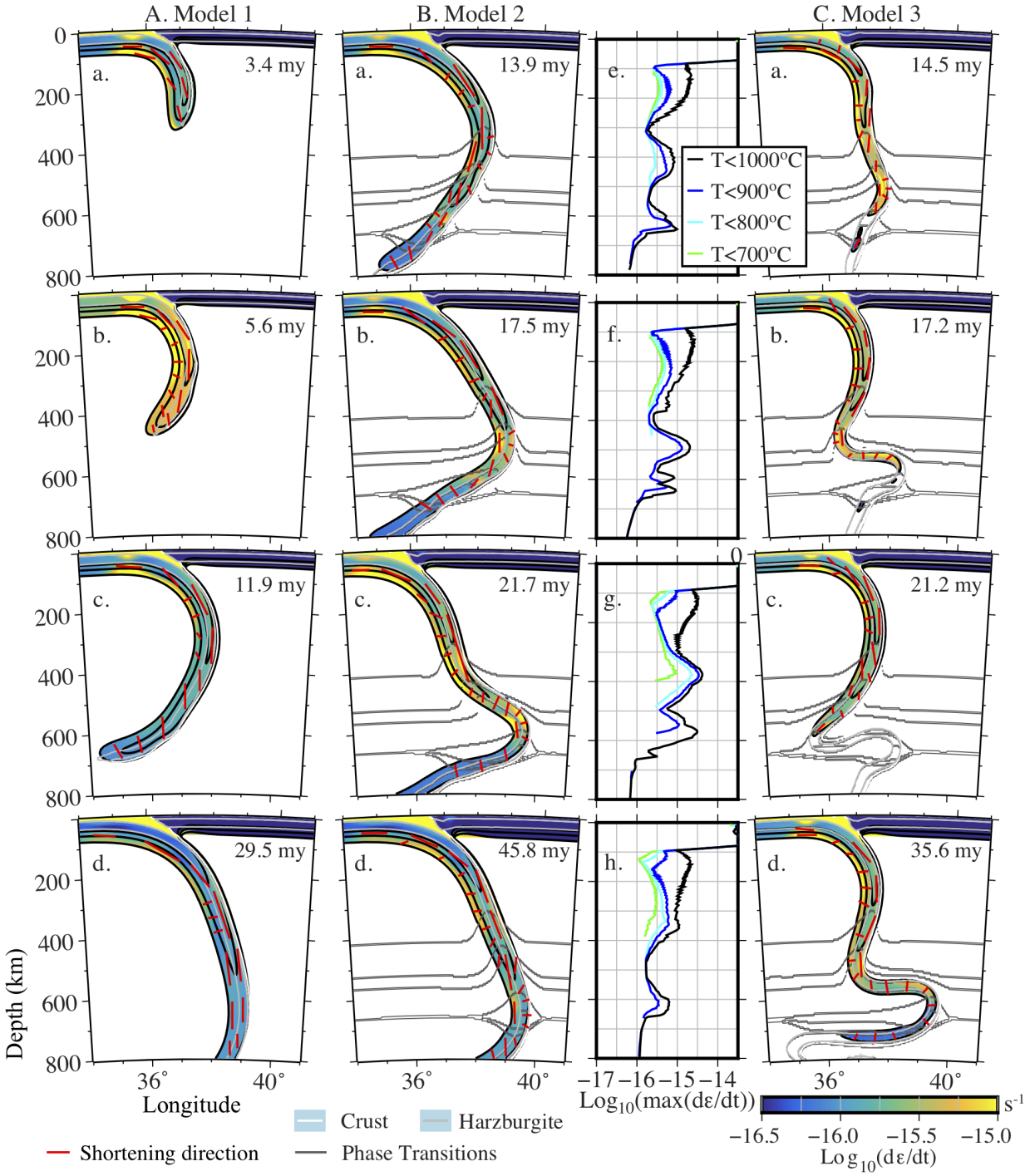

Figure 3: See caption next page.

Figure 3 *(previous page)*: In simulations of subduction, phase transitions cause folding and buckling of the slab leading to localized peaks of high strain-rate that change in time. Cross sections of subducted slab with strain-rate (color) within the 1000°C contour. Red bars indicate the pattern of shortening (compression) directions. **A.** Model 1 with no phase transitions shows little strain-rate variation in the slab. **B.** Model 2 with phase transitions has strong variations in strain-rate both spatially and temporally as the slab changes shape. **B, e–f** Depth profiles of the maximum strain-rate occurring below a specified temperature in the slab interior for Model 2 at the times shown in B, a–d. Colder temperature limits show the strain-rate at the interior of the slab. These strain-rate depth profiles are similar to the observed strain-rate profiles calculated from slab seismicity. **C.** Model 3, a younger slab (40 my) is a warmer and therefore weaker slab and deforms at higher strain-rates, but shows similar folding and buckling behavior to Model 2.

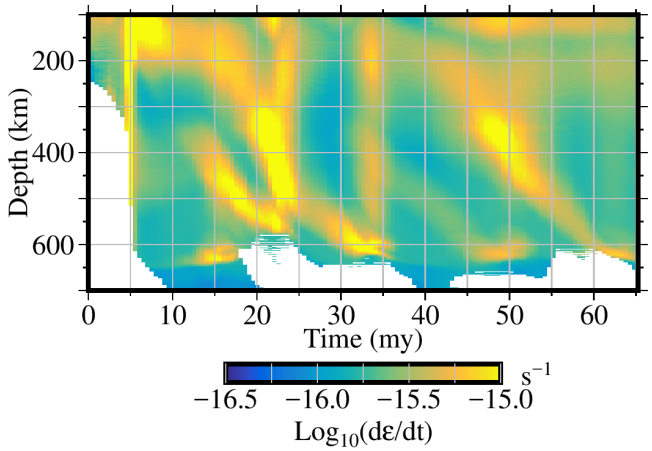

Figure 4: Time evolution of the maximum strain-rate in the slab for Model 2 demonstrates spatial and temporal variability. The color is the maximum strain-rate occurring in the slab at temperatures less than 900°C as a function of depth and simulation time. The depth and width of strain-rate peaks migrate in time following bending regions and folds. There is also a peak centered at 600 km depth that occurs at three times independent of a major fold in the slab (see Figure 5).

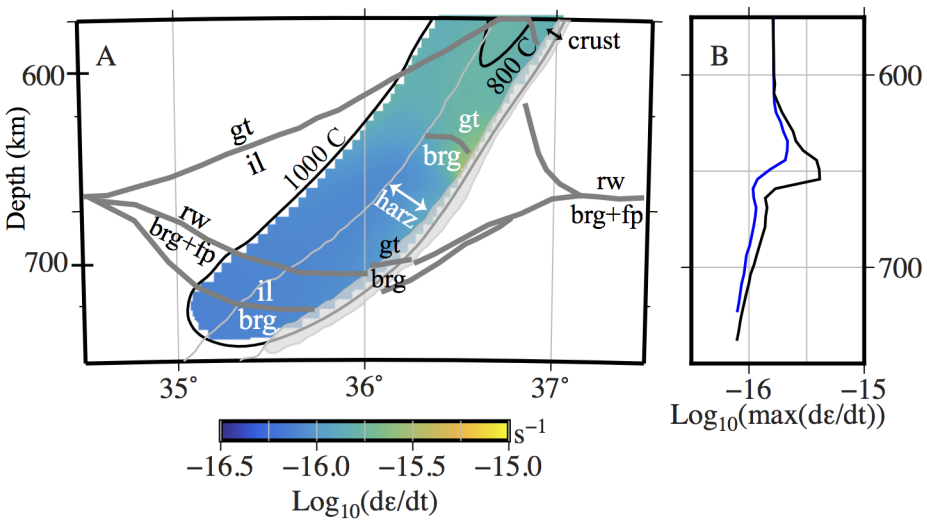

Figure 5: Strain-rate peak below 600 km depth is associated with garnet-to-Bridgmanite transition in the harzburgite layer. **A.** Zoom-in on Model 2 at 13.9 My (Figure 3E) showing the location of the phase transitions (gray), temperature contours (black) and strain-rate (color). **B.** Shows the profiles of the strain-rate peak at 1000°C (black) and 900°C (blue). This strain-rate peak occurs for periods of 5–10 my (see Figure 4) in the absence of significant folding or bending of the slab.

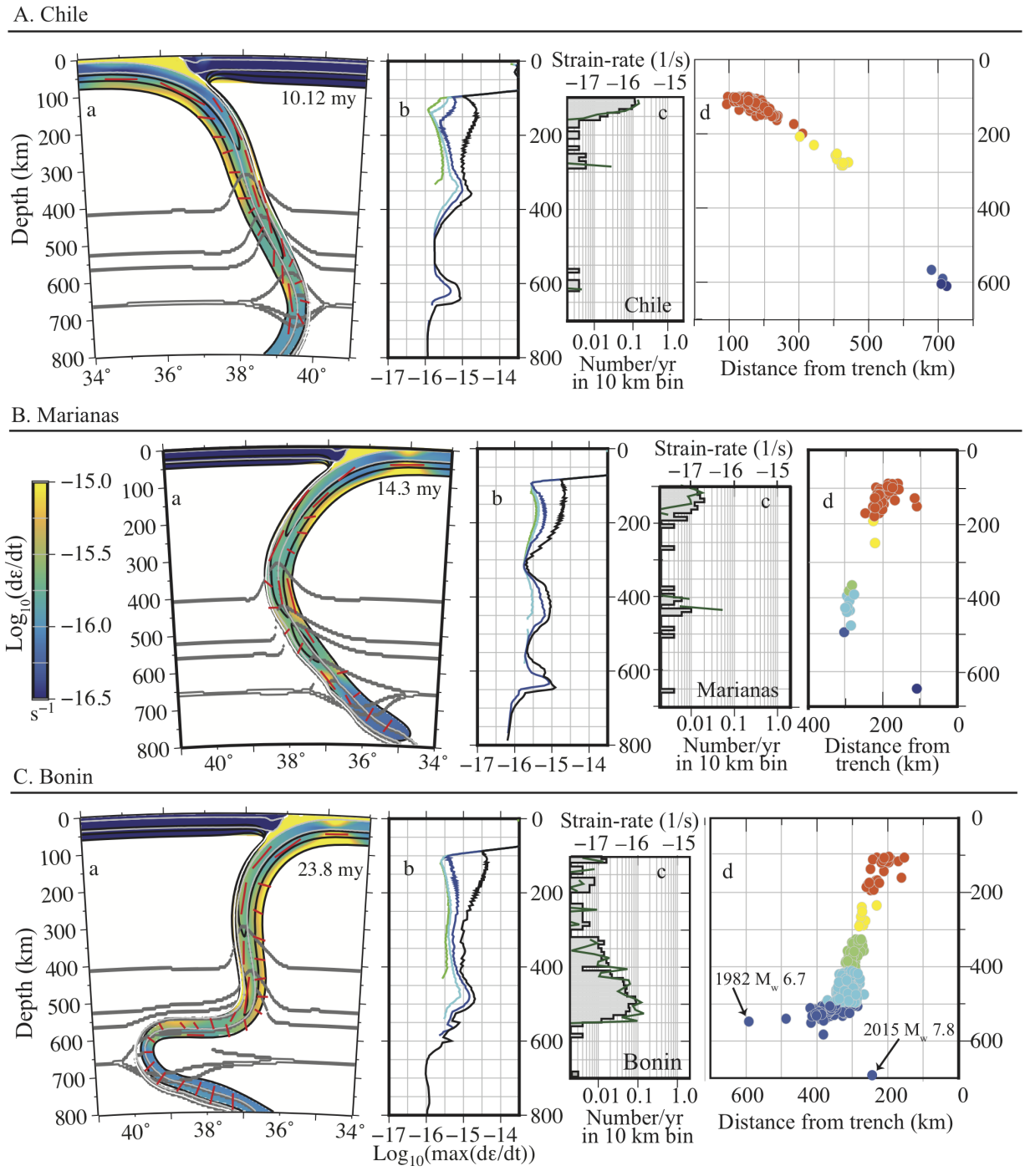

Figure 6: See caption next page.

Figure 6 *(previous page)*: Comparisons of model snap-shots and observations show similarities between slab shape and strain-rate distribution. Comparison for (**A**) the Chilean slab, (**B**) the Marianas slab, and (**C**) the Bonin slab. **a.** Snap-shots from Model 2 at times indicated. Colors and contours are the same as in Figure 3. **b.** Maximum strain-rate profiles. Line colors are the same as in Figure 3. **c.** Earthquake histogram and strain-rate for profile 7 in Chile, profile 7 in the Marianas, and profile 9 in Bonin. **d.** Cross section (depth vs. distance) of earthquakes for the same profile as the histograms. Colors indicate depth and are the same as used in Figure S2.

Supplemental Materials for:

Deep Slab Seismicity

Limited by Rate of Deformation in the Transition Zone

Magali I. Billen
Department of Earth and Planetary Sciences, U. C. Davis
mibillen@ucdavis.edu

Contents

Additional Supplemental Materials (Files uploaded separately)

1. Caption for Movie S1: Time evolution of Model 1 (80 my old subducting plate; no phase transitions).
2. Caption for Movie S2: Time evolution of Model 2 (80 my old subducting plate; with phase transitions).
3. Caption for Movie S3: Time evolution of Model 3 (40 my old subducting plate; with phase transitions).

1 Model Design Components

A summary of the model design components. For more details, including all of the parameters for the composite rheology and compositionally-dependent phase transitions see (*1–3*).

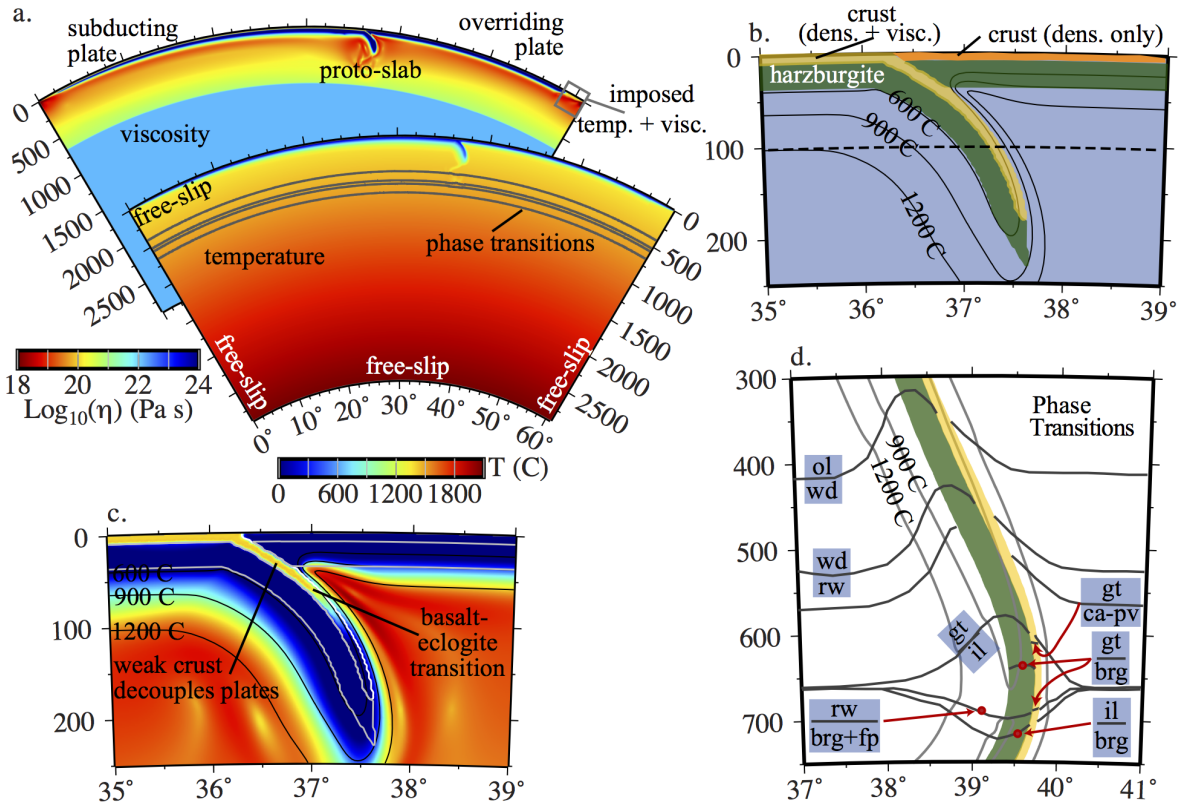

Figure S1: A summary of the model design components. a) Full Model domain showing initial viscosity and temperature structure, phase transitions and boundary conditions. Note 500 km wide box on trailing edge of overriding plate: the temperature and viscosity are reset in the box to allow for a mobile overriding plate and preventing formation of a subduction zone or maintaining the imposed mid-ocean ridge. b) Compositional layers and profile locations used to analyze the evolution of the temperature structure. Yellow layer: oceanic crust (basalt or eclogite density, fixed viscosity). Green layer: harzburgite with an olivine flow-law. Orange layer: oceanic crust (basalt density only). Light blue background: pyrolite composition with olivine flow law. c) Zoom-in on subduction plate boundary showing the viscosity structure for the proto-slab. Black contours are temperature. White contours outline the crust and harzburgite layers (shown in yellow and green in parts B and D). d) Zoom-in on the transition zone showing the compositionally-dependent phase transition boundaries across a sinking slab (snap-shot is from a model). Yellow/green layers are crust/harzburgite composition.

The initial thermal structure of the plates is defined by a half-space cooling model depending on plate age. For the subducting plate, the age increases from zero at the model boundary to either 40 or 80 my at the trench. For the overriding plate, the age increases from zero at the model boundary and reaches a maximum age of 20 my at 1000 km from the model boundary. The initial shape of the proto-slab is formed by running the model with fixed surface velocity boundary conditions (5 cm/yr) until the slab tip reached 200 km depth.

The composite visco-plastic rheology includes diffusion and dislocation creep mechanisms in the upper mantle, but only diffusion creep in the lower mantle. We use the olivine flow-law parameters modified for corrected water calibration and use of the second invariant of the strain-rate (see references in (*3*). Plastic deformation is modeled with a yield stress that increases with pressure up to a maximum value of 1000 MPa. This yield stress value sets the maximum strength of the slab of the cold interior of the slab. The value of the yield stress is chosen to match the expected stress during deformation through low temperature plasticity at the conditions in the slab. Other studies have shown that given the composite rheology used in our models, yield stress lower than 500 MPa results in break-off of the slab as it crosses through the phase changes at 410 km (*2*). Therefore, while some studies have concluded that the yield stress should be as low as 100 MPa, these models have a higher viscosity upper mantle and do not take into account the density due the phase transitions (*4*).

The overriding and subducting plates are separated by a 7.5 km thick low viscosity crustal layer (basalt) on the subducting plate. For the subducting plate this is modeled as weak layer, which then acts as the shear zone plate boundary and its location and dip are determined by the evolving dynamics in the simulation. The maximum viscosity of the weak crustal layer is 10^{20} Pa s. The crustal material also undergoes a phase transition from basalt to eclogite at depths of 50–150 km (depending on temperature), which also causes the viscosity to transition from that of the weak basalt to a viscosity for strong eclogite (modeled with the same flow law as for olivine) with a maximum viscosity of 10^{24} Pa s.

For each composition we assign appropriate proportions of pyroxene and olivine, and then track the phase transitions for both minerals. Inside the slab the compositionally-dependent phase transitions lead to 7 different phase transitions, each of which is associated with a density anomaly where the phase boundary is elevated or depressed due to the Clapeyron slope, as well as latent heat release.

2 Limitations of Model Design

Below I list the major limitations of the model design that are important to consider with respect to the magnitude of strain-rates, the distributions of strain-rate peaks, the level of stress in the slab and the ability to more directly link the long-term dynamics to the earthquake generation process.

1. The yield stress in the models is used to represent a variety of failure or plasticity processes that ultimately limit the strength of the crust and lithosphere. At shallow depth the yield stress is defined following Byerlee's law for brittle failure with an assumed pore pressure. This yield stress value increases linearly with depth up to the maximum value of 1 GPa at about 80 km depth. The maximum value is chosen to approximate the expected stress of deformation through low temperature plasticity, but is also, in effect, representing the long term approximation of any weakening process occurring in the slab. Including a better approximation of the Peierls flow-law (*5*) will likely allow for more deformation (higher strain-rate) at high stress in the cold interior of the slab. This would primarily change the magnitude of the strain-rates (making the larger), and it could also affect how slabs deform (e.g., curvature, amount of trench rollback). However, the correspondence of high strain-rate regions with regions of bending and buckling is expected to remain (*6*). Even with the addition of low-temperature plasticity, a yield strength may also be needed to approximate

other failure processes in the slab associated with deep earthquakes, just as the yield stress at shallow depths accounts for the long term effects of brittle deformation through frictional failure.

2. Elasticity is not included because the models consider the deformation of the slab over tens of millions of years. (*7*) present a systematic study of bending of a 3-D slab into the mantle as function of the viscous versus viscoelastic behavior. The main results of the study are that: 1) the mode of subduction and slab morphology are the same in viscous and visco-elastic models that have the same viscosity, 2) the energy is dissipated in different locations in visco-elastic slabs because some energy is stored elastically during bending and then released during unbending, 3) the location of the maximum stress in the bend will shift from the location of maximum bending rate (viscous) to location of maximum curvature (viscoelastic) because viscoelastic deformation is not co-axial, and 4) the magnitude of maximum stress is less in visco-elastic slabs because the elastic component allows more deformation at lower stress. This study confirms that the shape of bending in a sinking slab, and therefore the location of high strain-rate regions, is not expected to be affected by the lack of elasticity in the models. The location of maximum stress and the orientation of principal stresses, however, are affected by the lack of elasticity. Elasticity should be included in future models in order to more directly link the stress available in the models to the stress drops observed in deep earthquakes.

3. Phase transitions are modeled as occurring at the reference depth associated with a reference adiabat and pressure profile. This does not take into account tectonic overpressure associated with the phase transitions (*8*), or dynamic pressure due to the deformation of the slab itself (*9*). Both of these are expected to modified the net buoyancy contribution from the phase transitions.

4. The models do not include metastable olivine, which if present would lead to a different density structure within the slab and would affect the dynamic evolution of the slab (*10*). However, these models exhibit similar behavior to models under the same boundary conditions without a metastable olivine, except that the sinking velocity is more oscillatory in time. Therefore, one can expect that a MO wedge will modify sinking rates, but that the bending and buckling behavior will continue to be controlled by the phase transitions and viscosity increase at 660 km, and the rheology of the slab.

5. The models are incompressible and therefore do not account for the deformation associated with the phase transitions themselves (*8, 11*), nor how this changes pressure locally (*9*). Both of these effects will modify the depth of the phase transitions and can lead to large down-dip compressional stresses caused by the volume contraction of the higher pressure phase compared to the the olivine (*12*).

6. These models are fully-dynamic, which is not usually thought of as a limitation. However, it limits comparison between the models and specific regions because the subduction rate and trench motion are free to evolve. Models designed for comparison to specific locations would need to prescribe observed past plate and trench motion in order to better reproduce the present-day shape of slabs.

7. The models are two-dimensional, which again limits how we can compare these models to observations. The stress distribution will also vary along strike in 3D models, in particular as bending and buckling propagates along strike.

3 Earthquakes Maps and Profiles

The following figures (S2A–H) show the earthquakes used in to examine slab shape and to calculate the seismic strain-rate. Earthquakes were downloaded from the EHB-ISC catalog for $M >= 4$, at depths of 100– 700 km, for 1964–2014 (*13, 14*). Also plotted for reference are the orientation of the P-axis (principal shortening direction) for earthquakes also listed in the global CMT catalog (*15, 16*).

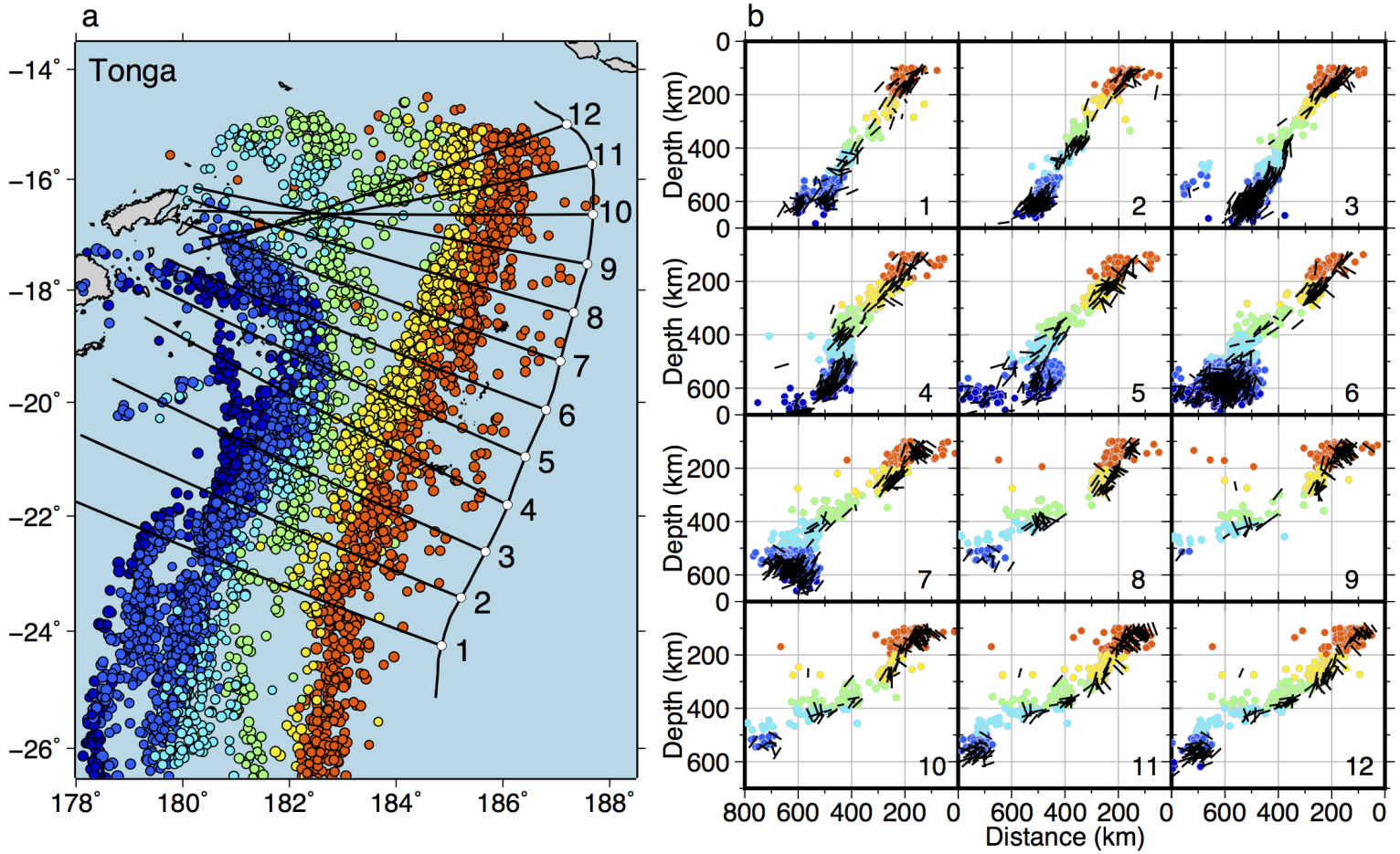

Figure S2A: Earthquakes, profiles and P-axis for Tonga. a. Map of earthquake location colors correspond to the depth as shown in b. Black lines indicate the location for each trench-perpendicular profile (100 km spacing). b. Trench perpendicular distance-depth profiles of earthquakes located within ± 50 km of the profiles (each profile is numbered). Black bars indicate the orientation of the principal shortening direction from available CMT solutions.

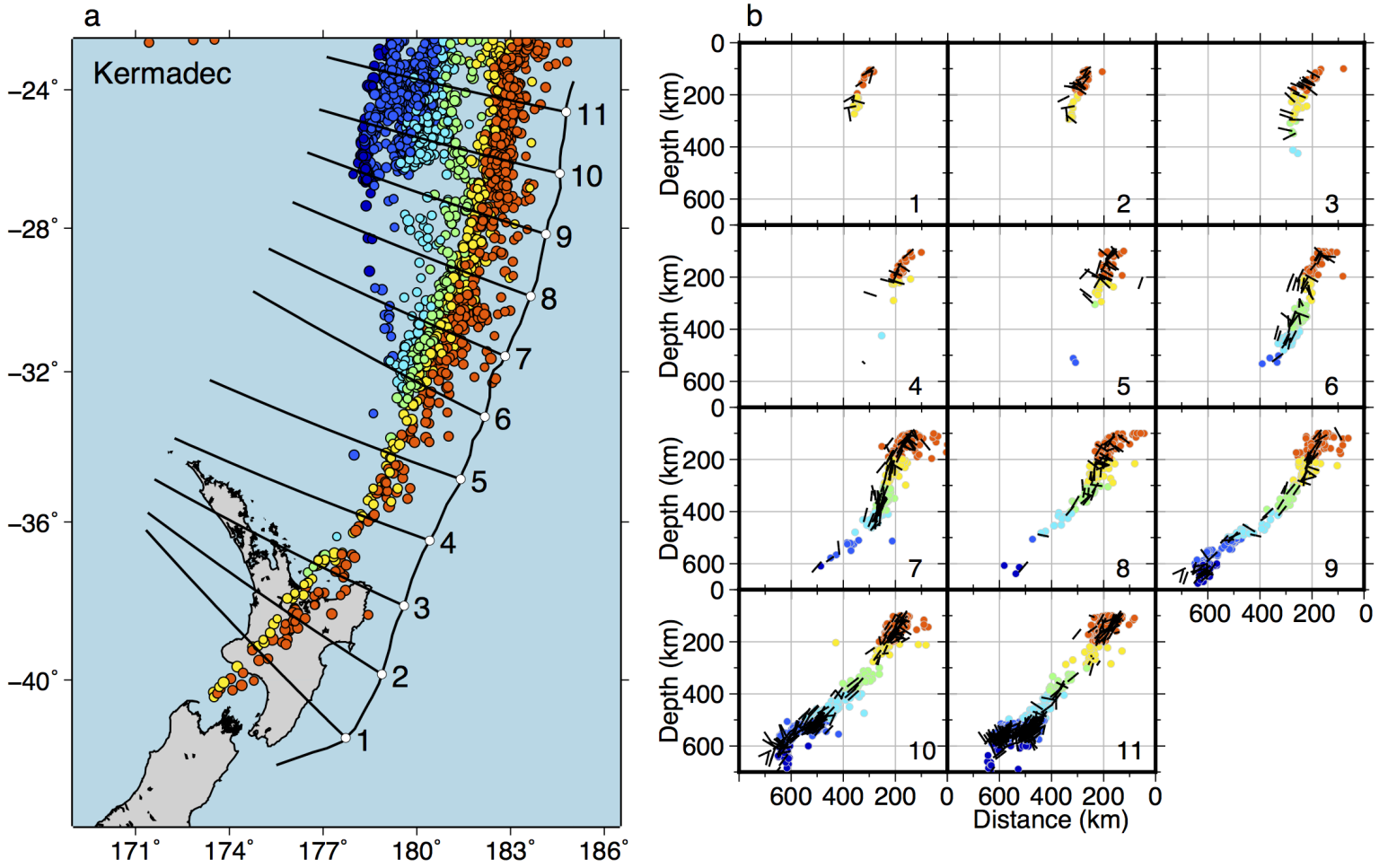

Figure S2B: Earthquakes, profiles and P-axis for Kermadec. Profile spacing of 200 km. Earthquakes plotted within ±100 km of the profiles.

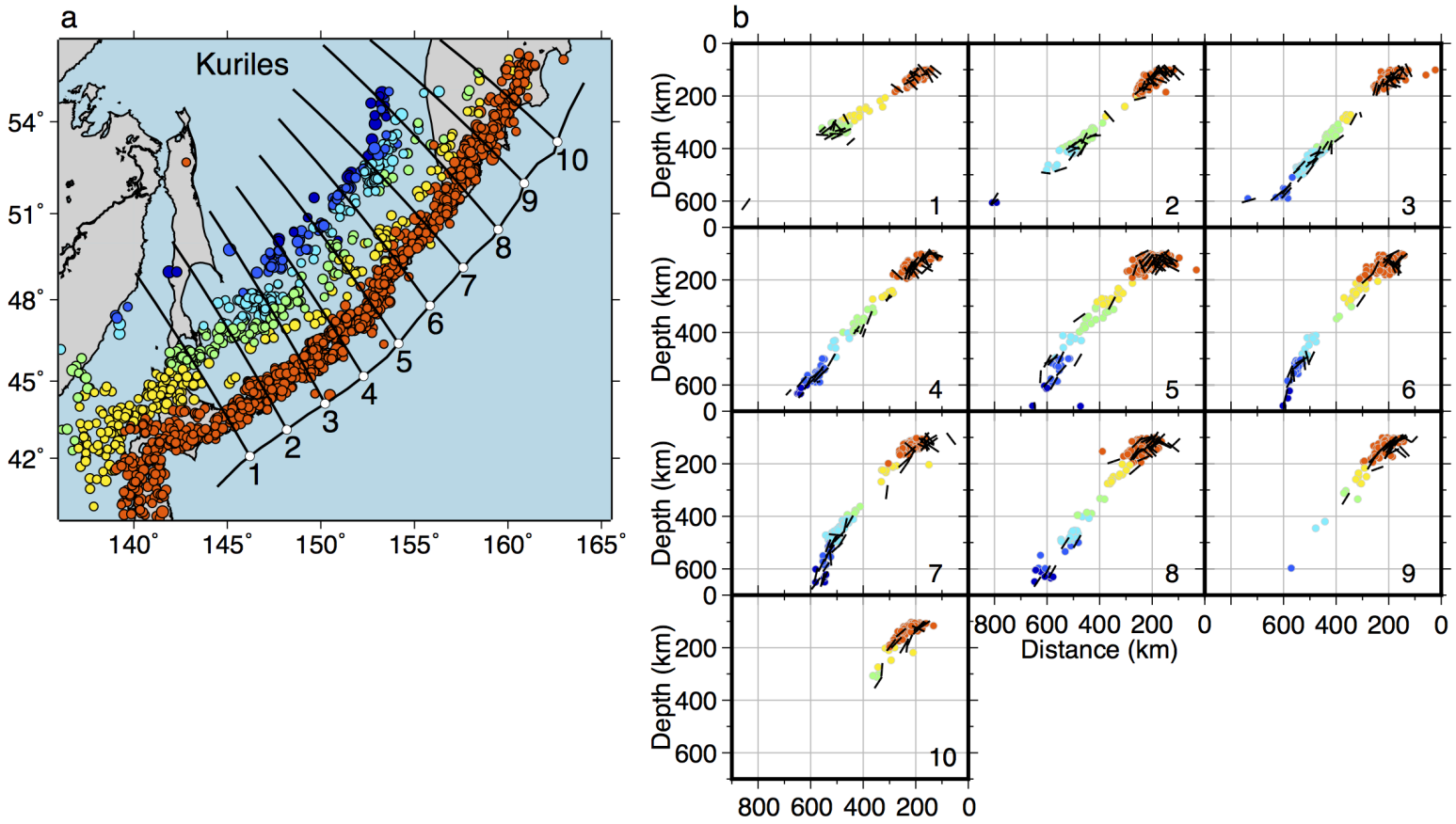

Figure S2C: Earthquakes, profiles and P-axis for Kuriles. Profile spacing of 200 km. Earthquakes plotted within ± 100 km of the profiles.

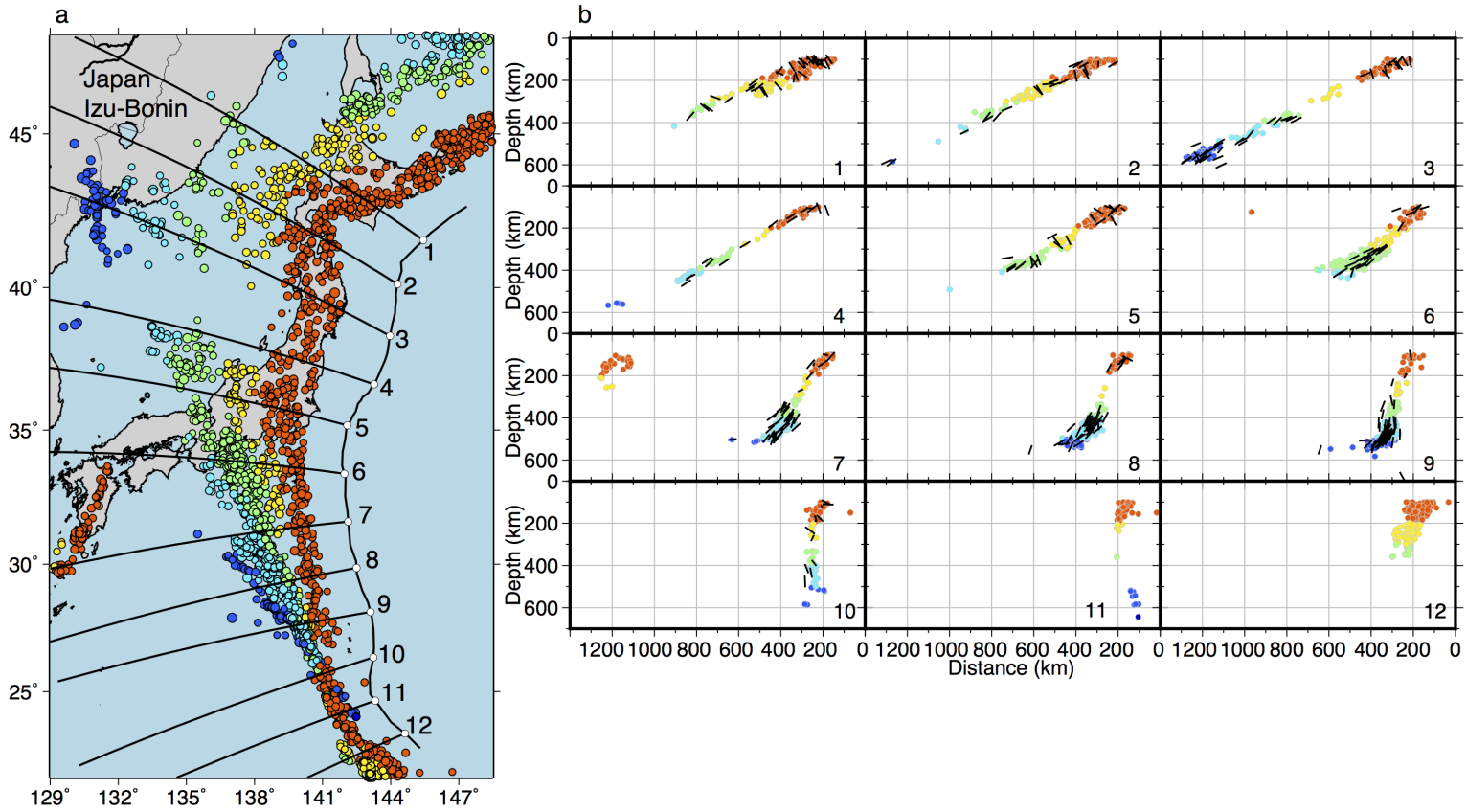

Figure S2D: Earthquakes, profiles and P-axis for Japan. Profile spacing of 200 km. Earthquakes plotted within ± 100 km of the profiles.

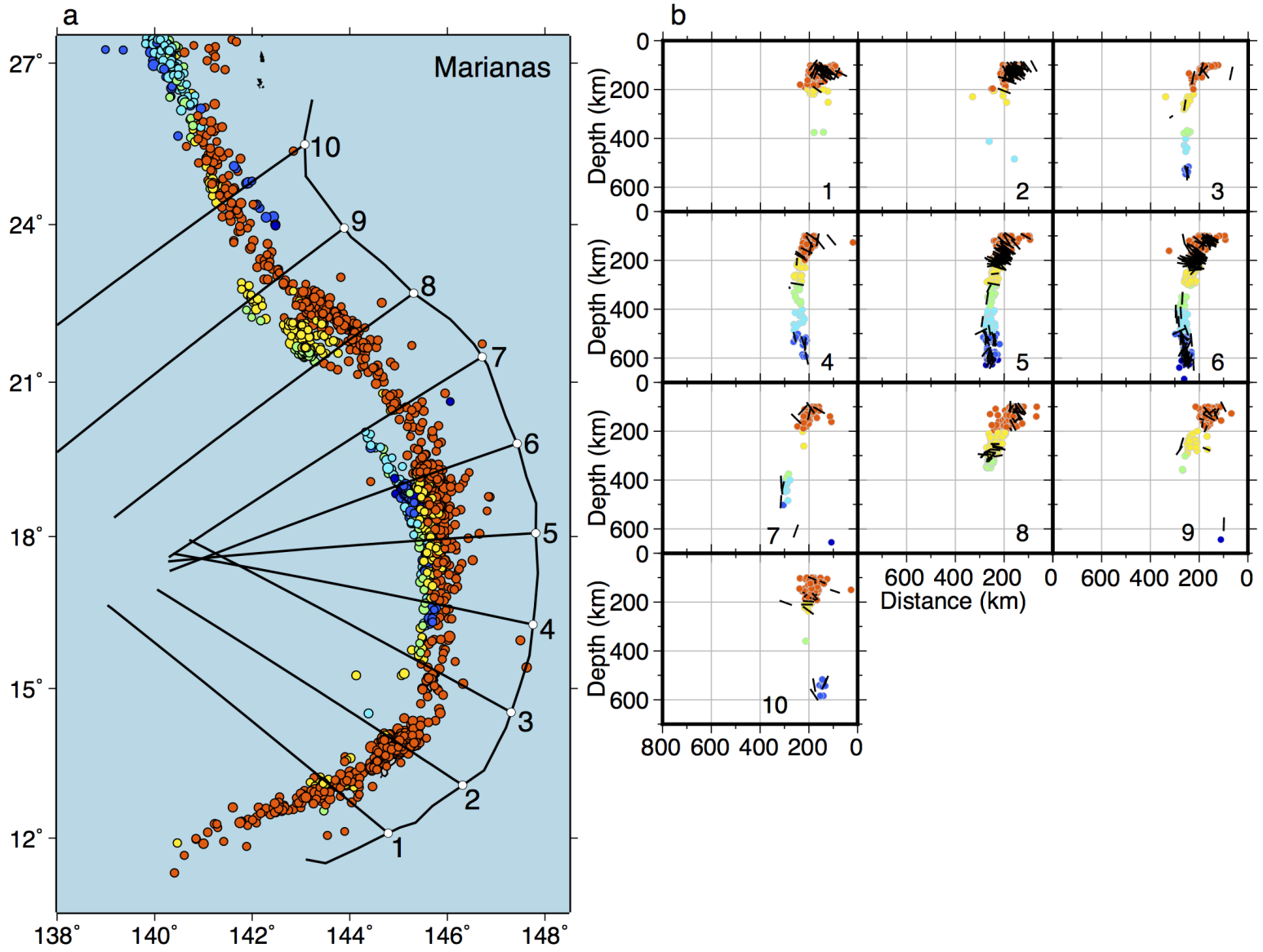

Figure S2E: Earthquakes, profiles and P-axis for Marianas. Profile spacing of 200 km. Earthquakes plotted within ± 100 km of the profiles.

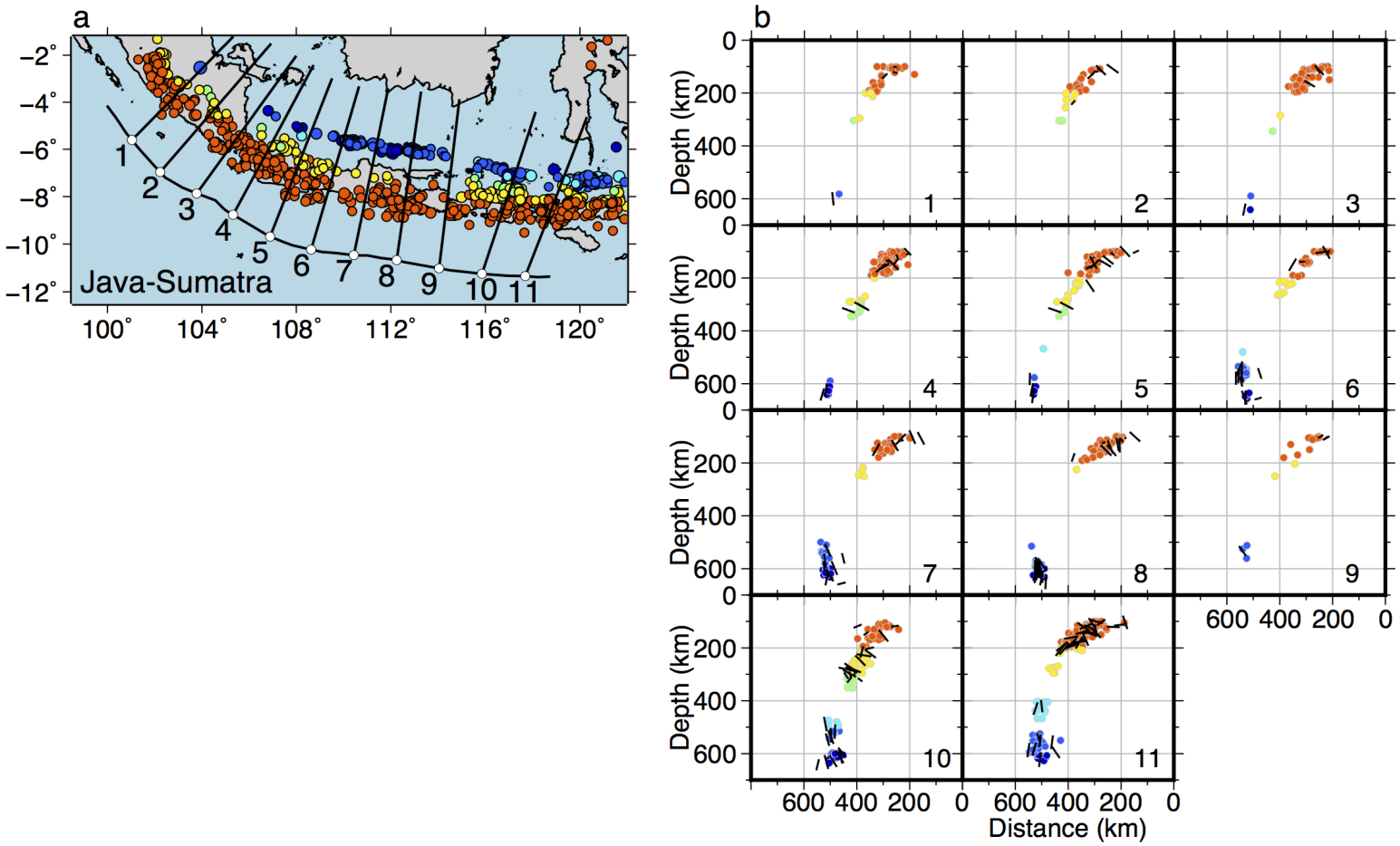

Figure S2F: Earthquakes, profiles and P-axis for Java-Sumatra. Profile spacing of 200 km. Earthquakes plotted within ±100 km of the profiles.

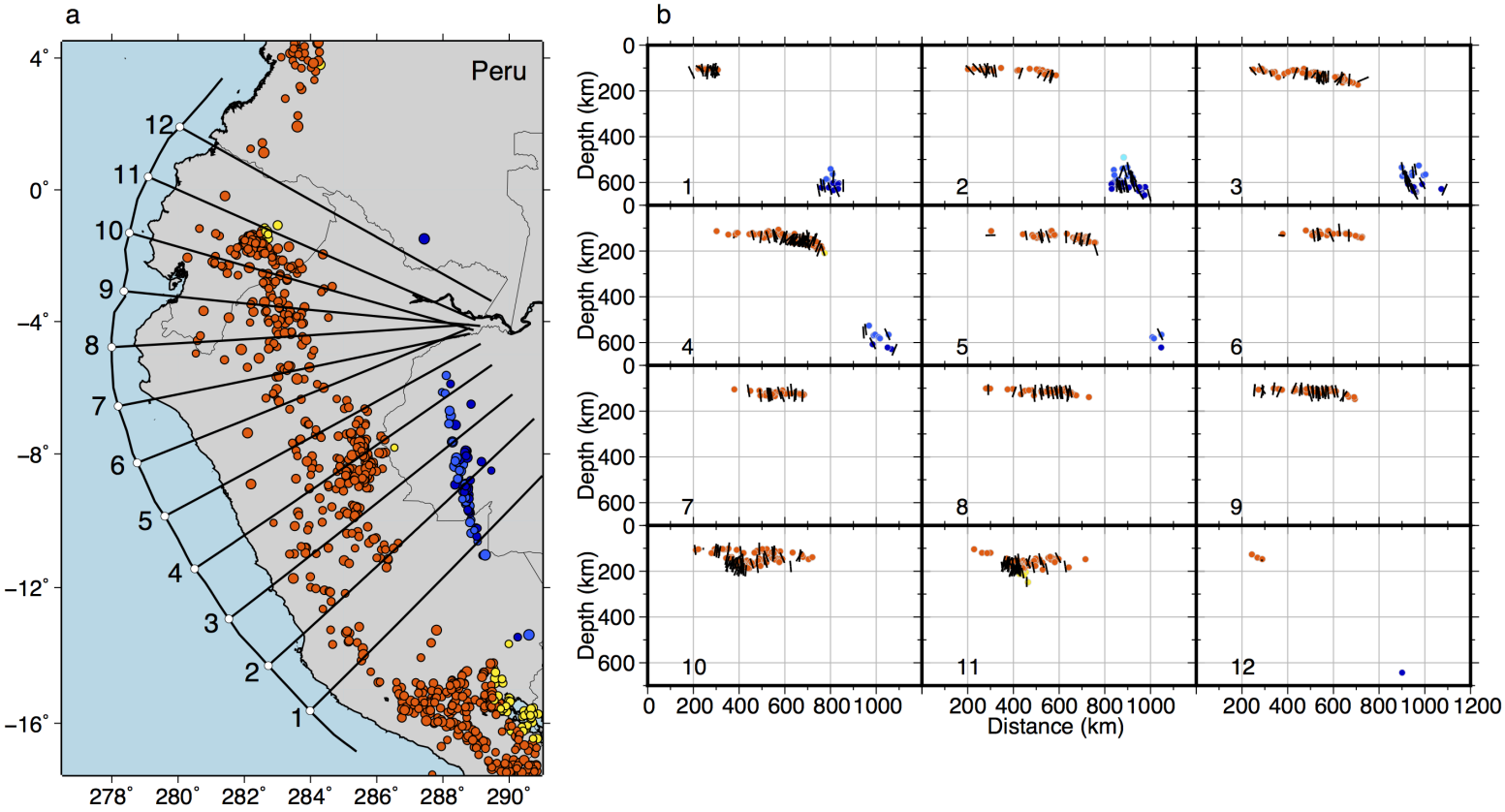

Figure S2G: Earthquakes, profiles and P-axis for Peru. Profile spacing of 200 km. Earthquakes plotted within ± 100 km of the profiles.

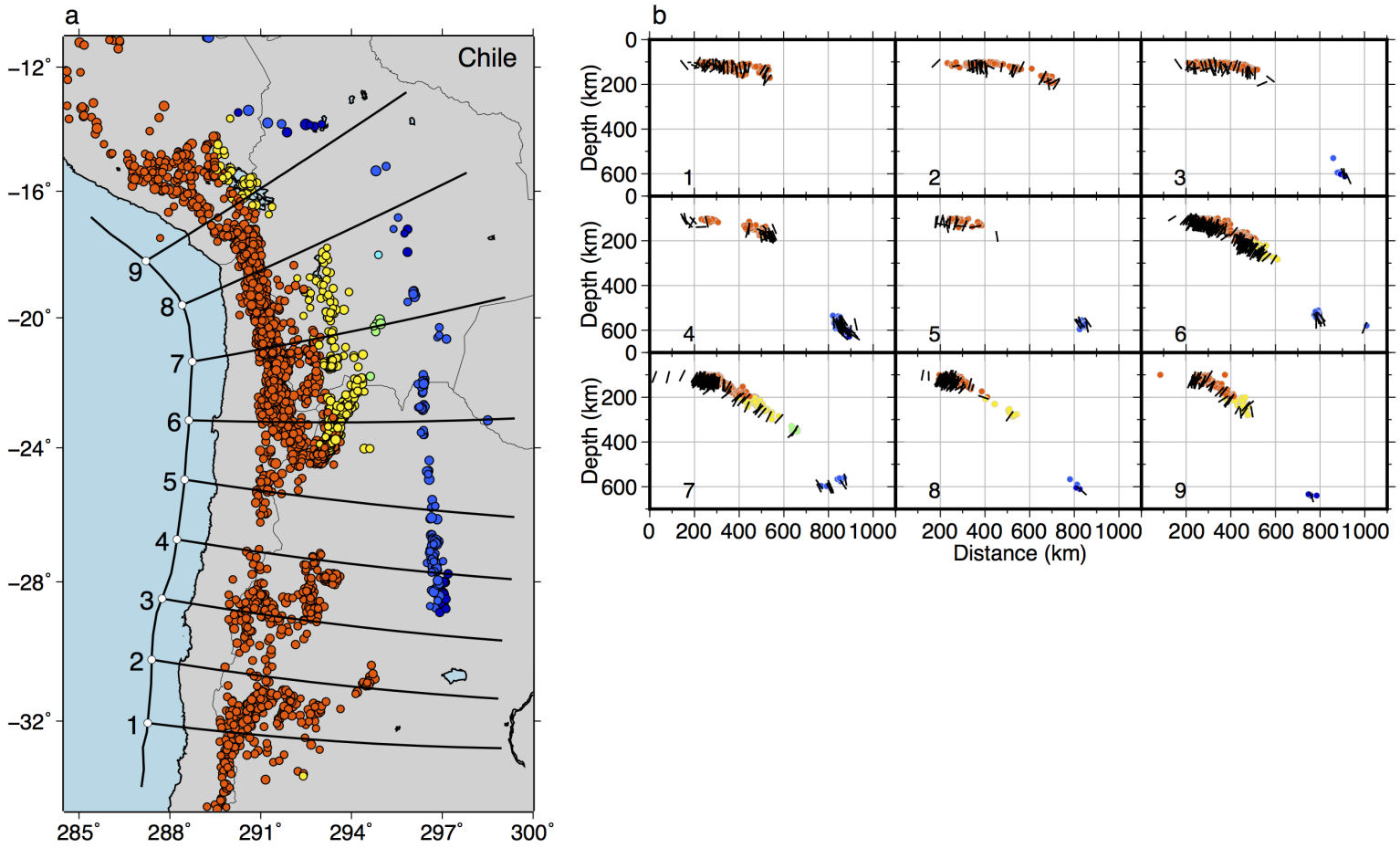

Figure S2H: Earthquakes, profiles and P-axis for Chile. Profile spacing of 200 km. Earthquakes plotted within ± 100 km of the profiles.

4 Seismicity and Strain-rate Profiles

The following figures (S3A–H) show the seismicity rate (number/10 km bin/year) and strain-rate along trench-perpendicular profiles for each region. The seismicity is the total number of earthquakes within depth bins divided by bin width (10 km) and divided by the period of time the earthquakes were recorded (50 years). For each profile the earthquakes within ± 100 km (± 50 km for Tonga) are considered. The regional profile is found by adding up each of the trench-parallel profiles. The strain-rate is calculate following (*17*) as explained above in section S3.

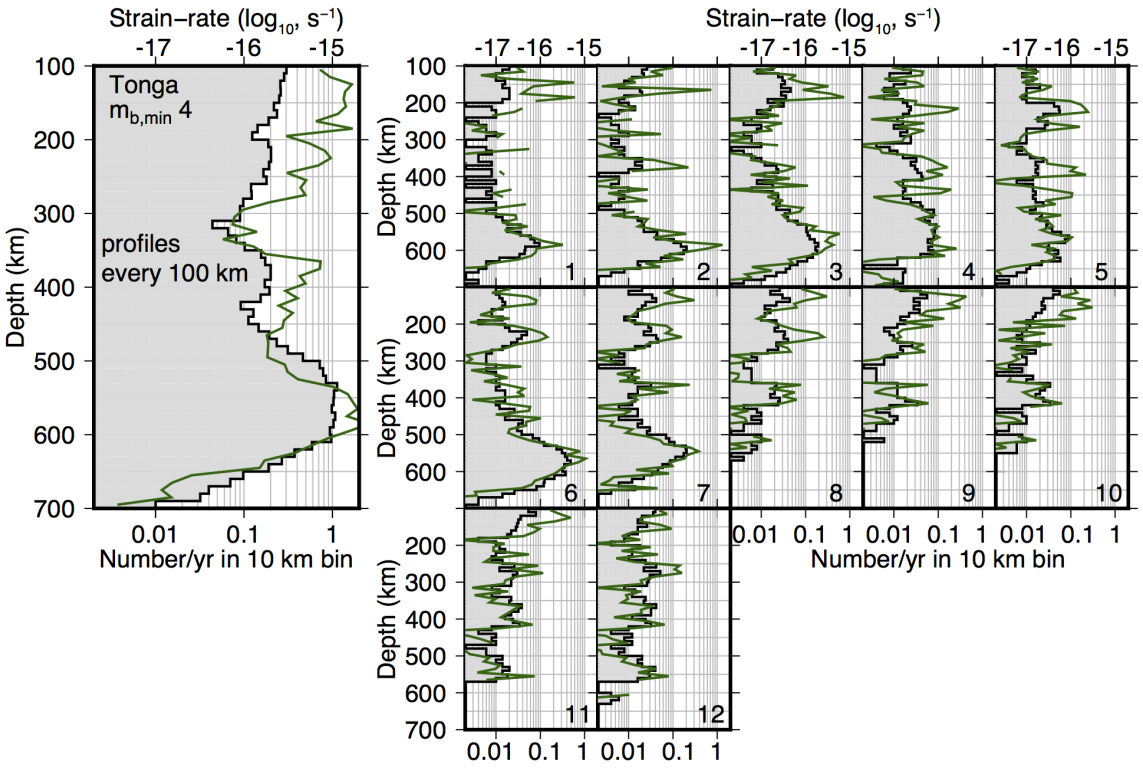

Figure S3A: Seismicity rate and strain-rate for Tonga. Location of trench-perpendicular profiles and earthquakes used in the calculation are show in Figure S2A.

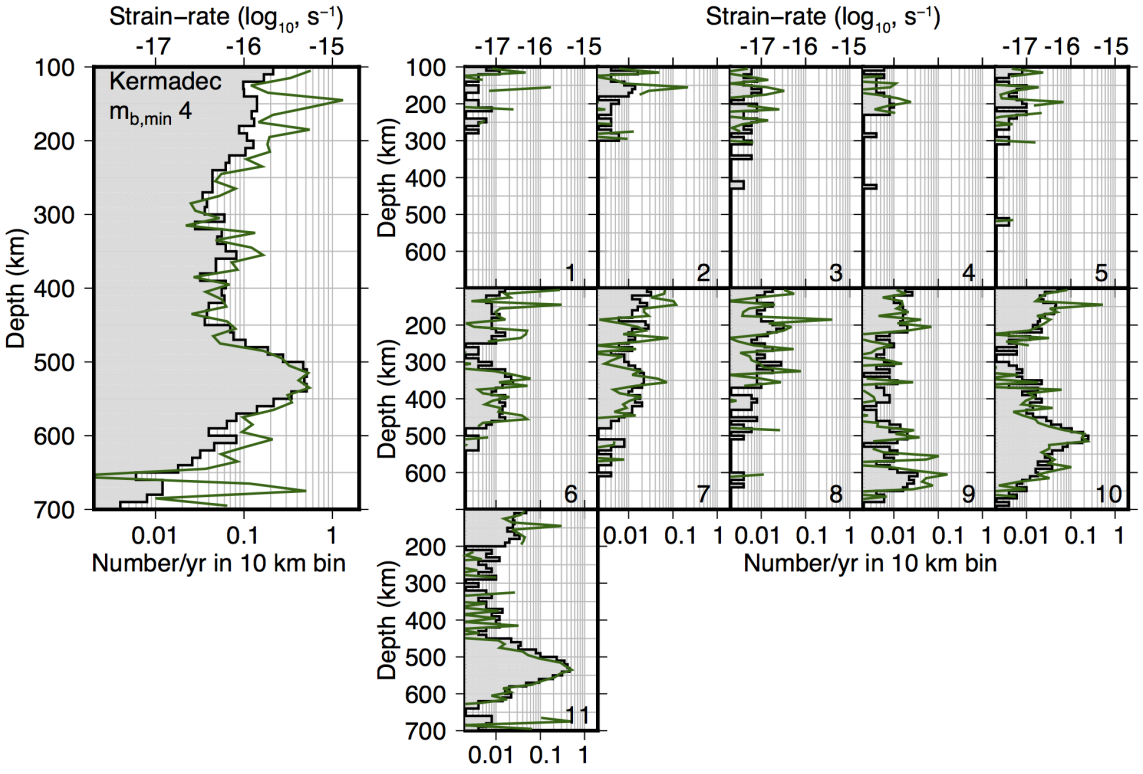

Figure S3B: Seismicity rate and strain-rate for Kermadec. Location of trench-perpendicular profiles and earthquakes used in the calculation are show in Figure S2B.

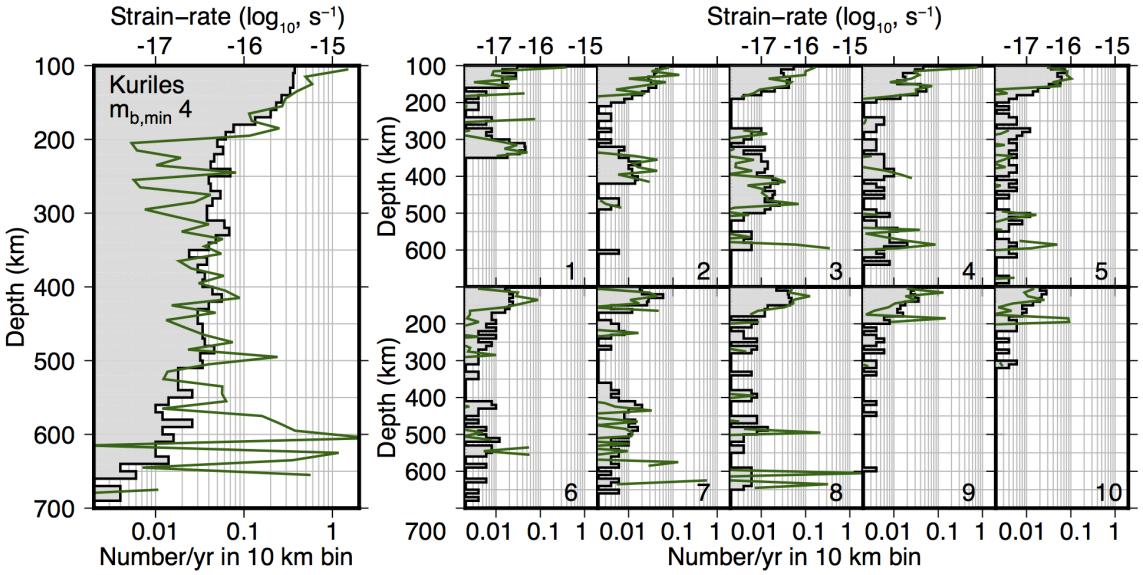

Figure S3C: Seismicity rate and strain-rate for Kuriles. Location of trench-perpendicular profiles and earthquakes used in the calculation are show in Figure S2C.

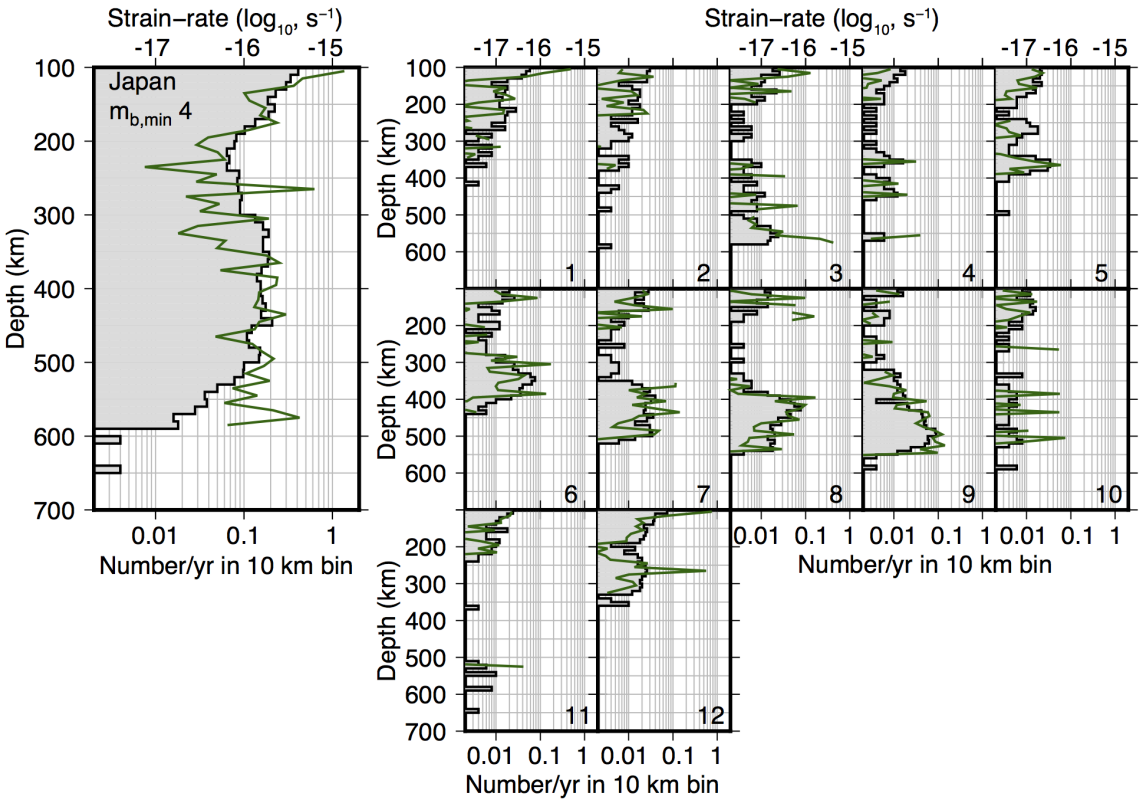

Figure S3D: Seismicity rate and strain-rate for Japan. Location of trench-perpendicular profiles and earthquakes used in the calculation are show in Figure S2D.

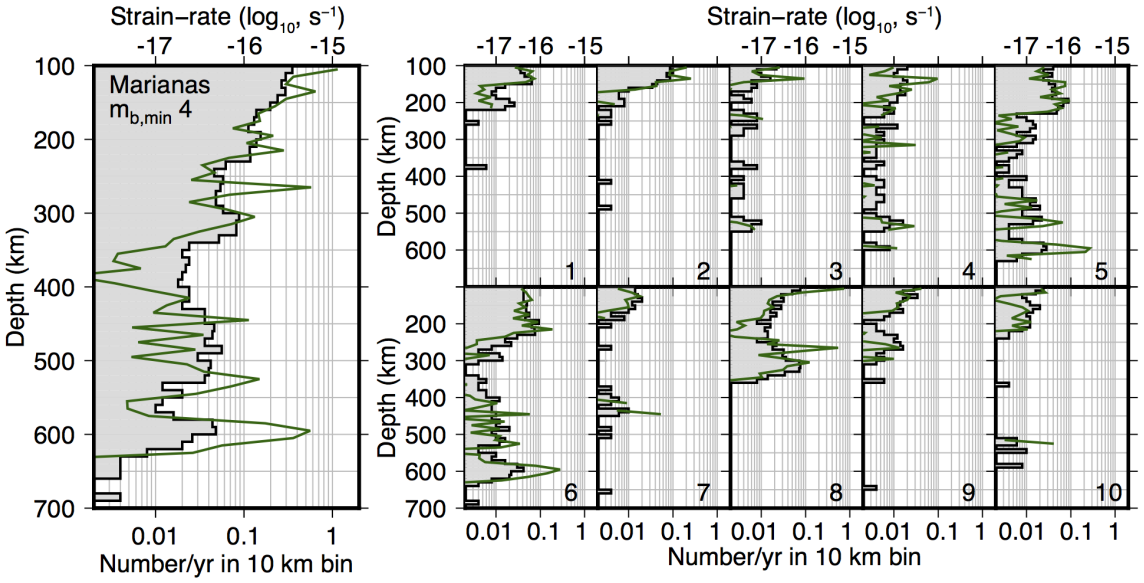

Figure S3E: Seismicity rate and strain-rate for Marianas. Location of trench-perpendicular profiles and earthquakes used in the calculation are show in Figure S2E.

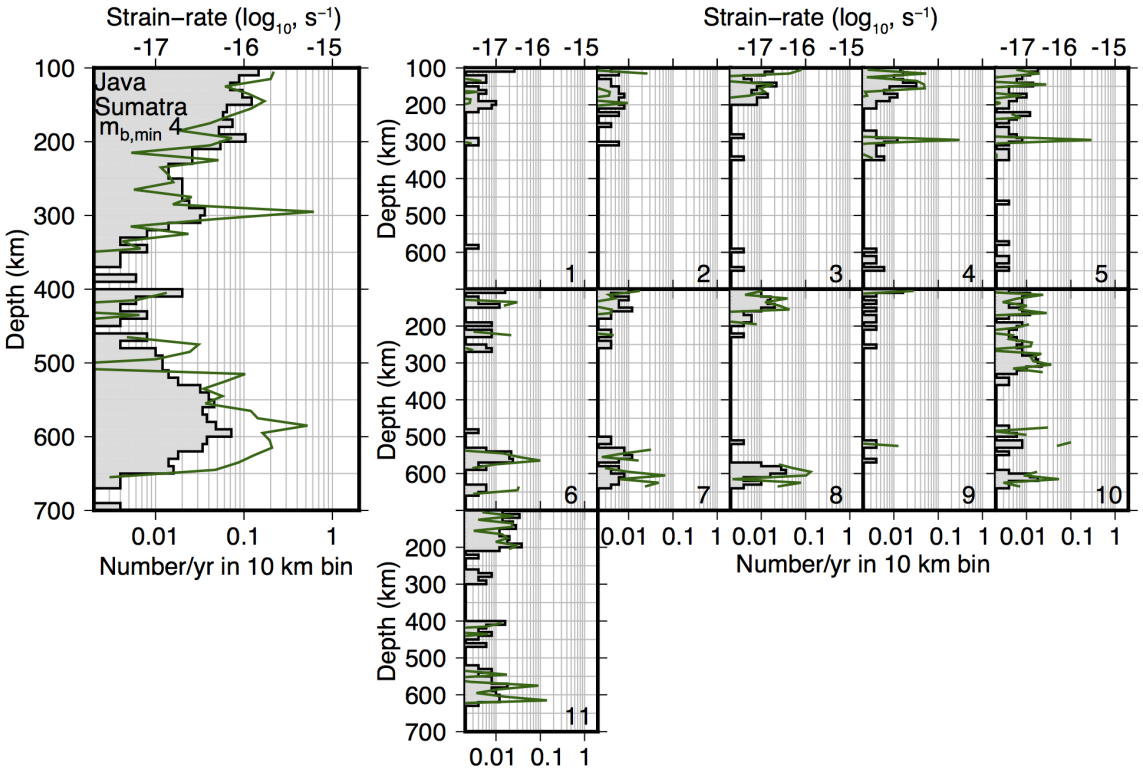

Figure S3F: Seismicity rate and strain-rate for Java-Sumatra. Location of trench-perpendicular profiles and earthquakes used in the calculation are show in Figure S2F.

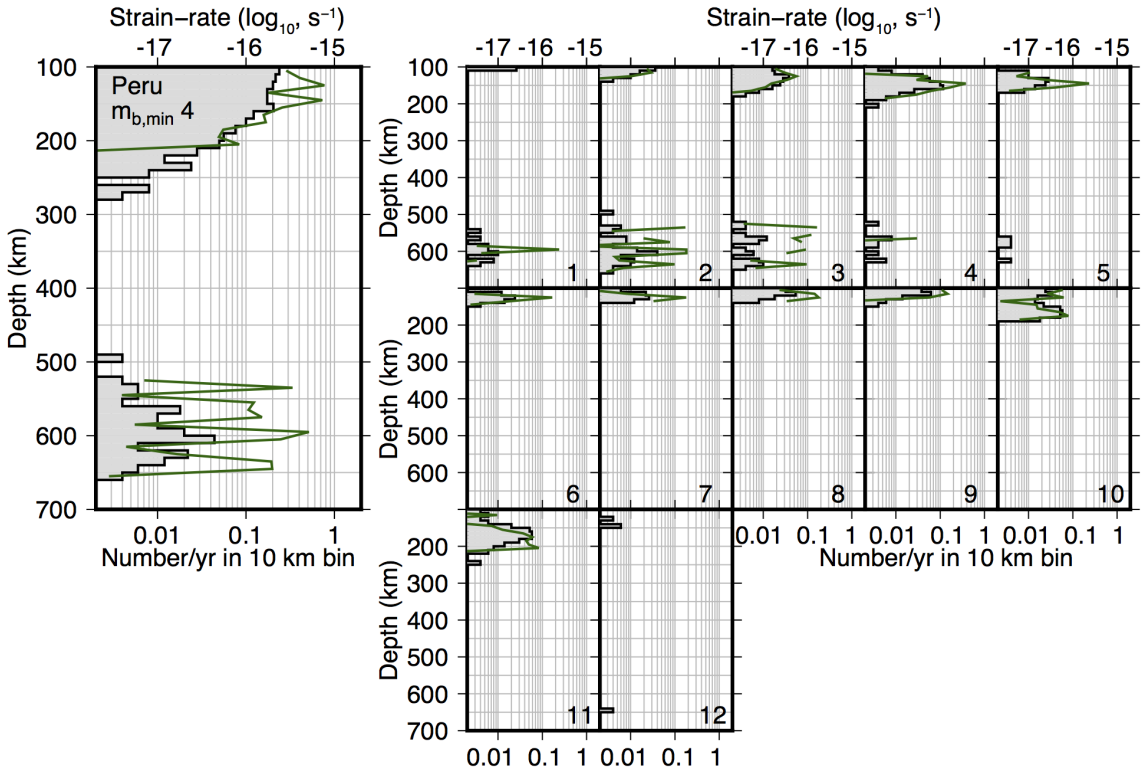

Figure S3G: Seismicity rate and strain-rate for Peru. Location of trench-perpendicular profiles and earthquakes used in the calculation are show in Figure S2G.

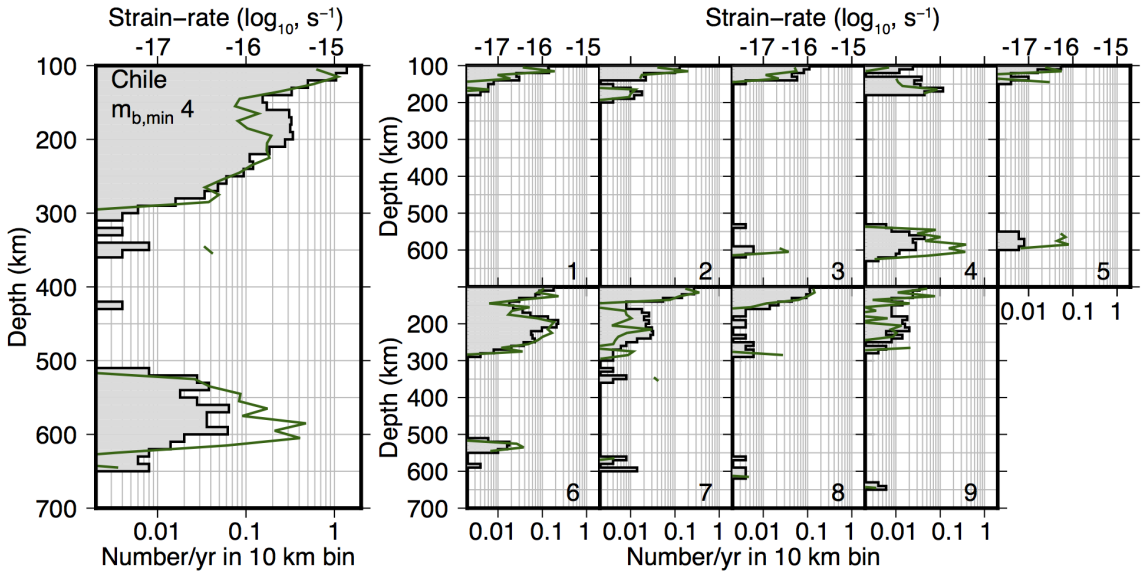

Figure S3H: Seismicity rate and strain-rate for Chile. Location of trench-perpendicular profiles and earthquakes used in the calculation are show in Figure S2H.

Movie S1: Time evolution of Model 1 (80 my old subducting plate; no phase transitions).

With no phase transitions, there is not folding and buckling and the strong slab undergoes very little internal deformation. The strain-rate decreases with depth. Label at the top-right corner of the movie indicates model parameters. Left: Color image is viscosity ($\log_{10}(\eta)$) with temperature contour every 300°C (thin black line), outlines of the crust and harzburgite layers (thin white lines), and solid flow velocity vectors (white arrows). Gray bar above the surface at 36.0° indicates starting position of trench; red bar indicates trench position for the time shown in the frame. Middle: Color image is second invariant of the strain-rate ($\log_{10}(\dot{\epsilon})$) plotted within the 1000°C temperature contour). Right: maximum strain-rate as function of depth found within a specific temperature contour.

Movie S2: Time evolution of Model 2 (80 my old subducting plate; with phase transitions)

Phase transitions lead to time-dependent folding and buckling of the slab, which in results in time-variable strain-rate-depth profiles in the slab. Depth of high strain-rate regions migrates with time. Label at the top-right corner of the movie indicates model parameters. Left: Color image is viscosity ($\log_{10}(\eta)$) with temperature contour every 300°C (thin black line), outlines of the crust and harzburgite layers (thin white lines), and solid flow velocity vectors (white arrows). Gray bar above the surface at 36.0° indicates starting position of trench; red bar indicates trench position for the time shown in the frame. Middle: Color image is second invariant of the strain-rate ($\log_{10}(\dot{\epsilon})$) plotted within the 1000°C temperature contour). Right: maximum strain-rate as function of depth found within a specific temperature contour.

Movie S3: Time evolution of Model 3 (40 my old subducting plate; with phase transitions)

Similar to Model 2, but with a younger (warmer) slab, there are higher strain-rates recorded in the thinner and weaker slab interior. Note that subduction rate slows with time and the slab age therefore also increases for later model times. Label at the top-right corner of the movie indicates model parameters. Left: Color image is viscosity ($\log_{10}(\eta)$) with temperature contour every 300°C (thin black line), outlines of the crust and harzburgite layers (thin white lines), and solid flow velocity vectors (white arrows). Gray bar above the surface at 36.0° indicates starting position of trench; red bar indicates trench position for the time shown in the frame. Middle: Color image is second invariant of the strain-rate ($\log_{10}(\dot{\epsilon})$) plotted within the 1000°C temperature contour). Right: maximum strain-rate as function of depth found within a specific temperature contour.

References

1. K. Arredondo, M. I. Billen, The effects of phase transitions and compositional layering in two-dimensional kinematic models of subduction. *Journal of Geodynamics* **100**, 159-174 (2016).

2. K. M. Arredondo, M. I. Billen, Coupled effects of phase transitions and rheology in 2D dynamical models of subduction. *Journal of Geophysical Research* **122**, 5813-5830 (2017).

3. M. I. Billen, K. M. Arredondo, Decoupling of plate-asthenosphere motion caused by nonlinear viscosity during slab folding in the transition zone. *Physics of the Earth and Planetary Interiors* **281**, 17-30 (2018).

4. L. Alisic, M. Gurnis, G. Stadler, C. Burstedde, L. C. Wilcox, O. Ghattas, Slab stress and strain rate constraining global mantle flow. *Geophysical Research Letters* **32** (2010).

5. M. Kameyama, D. A. Yuen, S.-I. Karato, Thermal-mechanical effects of low-temperature plasticity (the Peierls mechanism) on the deformation of a visco-elastic shear zone. *Earth and Planet. Sci. Lett.* **168**, 159-172 (1999).

6. F. Garel, S. Goes, D. R. Davies, J. H. Davies, S. C. Kramer, C. R. Wilson, Interaction of subducted slabs with the mantle transition-zone: A regime diagram from 2-D thermo-mechanical models with a mobile trench and an overriding plate. *Geochemistry, Geophysics, Geosystems* **15**, 1739–1765 (2014).

7. R. J. Farrington, L.-N. Moresi, F. A. Capitanio, The role of viscoelasticity in subducting plates. *Geochemistry Geophysics Geosystems* **15**, 4191-4304 (2014).

8. B.-D. So, D. A. Yuen, Generation of tectonic over-pressure inside subducting oceanic lithosphere involving phase-loop of olivine–wadsleyite transition. *Earth and Planetary Science Letters* **413** (2015).

9. R. Gassmöller, J. Dannberg, W. Bangerth, T. Heister, R. Myhill, Capturing dynamic effects of compressible mantle convection: New formulations and numerical methods (DI33C-0049), Presented at the 2019 Fall Meeting, AGU, San Francisco, CA 9-13 Dec. (2019).

10. M. Tetzlaff, H. Schmeling, Time-dependent interaction between subduction dynamics and phase transition kinetics. *Geophysical Journal International* **178**, 826-844 (2009).

11. A. Guest, G. Schubert, C. W. Gable, Stress field in subducting lithosphere and comparison with deep earthquakes in Tonga. *Journal of Geophysical Research* **108**, 2288 (2003).

12. J. P. Devaux, L. Fleitout, G. Schubert, C. Anderson, Stresses in a subducting slab in the presence of a metastable olivine wedge. *Journal of Geophysical Research* **105**, 13365-13373 (2000).

13. ISC-EHB, The ISC-EHB Bulletin 1960–2014, www.isc.ac.uk/isc-ehb/, last accessed on November 26 (2018).

14. E. R. Engdahl, R. van der Hilst, R. Buland, Global teleseismic earthquake relocation with improved travel times and procedures for depth determination. *Bulletin of the Seismological Society of America* **88**, 722-743 (1998).

15. CMT-Catalog, Global centroid moment tensor catalog, www.globalcmt.org, last accessed on December 1 (2018).

16. G. Ekström, M. Nettles, A. M. Dziewonski, The global CMT project 2004-2010: Centroid-moment tensors for 13,017 earthquakes. *Physics of the Earth and Planetary Interiors* **200-201** (2012).

17. M. Bevis, Seismic slip and down-dip strain rates in Wadati-Benioff Zones. *Science* **240**, 1317-1319 (1988).